The G^0 Experiment
Backward Angle Measurements
Update

The G^0 Collaboration

California Institute of Technology, Carnegie-Mellon University, College of William and Mary, Hampton University, L'Institut de Physique Nucléaire d'Orsay, Laboratoire de Physique Subatomique et de Cosmologie Grenoble, Louisiana Tech. University, New Mexico State University, Thomas Jefferson National Laboratory, TRIUMF, University of Connecticut, University of Illinois at Urbana-Champaign, University of Kentucky, University of Manitoba, University of Maryland, University of Massachusetts, University of Northern British Columbia, Virginia Tech, and Yerevan Physics Institute

May 2004

Contents

1 Summary

This submission regarding the G^0 experiment has been prepared for consideration by the Jefferson Lab Program Advisory Committee at its PAC26 meeting. The G^0 experiment has been approved previously at four PAC meetings (as 91-017 in December 1993, 99-016 in January 99, 00-006 in January 00 and 01-116 in July 01); these approvals have covered the experiment commissioning, the forward angle running and conditional approval for the first backward angle measurement. *As E01-116 is not on the firm schedule, we request reapproval of the first backward angle measurement in the context of the standard JLab jeopardy framework. We also request that the PAC reconsider the 10 days of commmissioning time specifically for the backward angle run requested, but not approved, in our previous proposal.*

In the G^0 experiment, parity-violating asymmetries in elastic electron scattering from the nucleon will be measured at both forward and backward angles and over a range of momentum transfers from about 0.1 – 1.0 $\mathrm{GeV}^2/\mathrm{c}^2$. The primary purpose of the experiment is to separate the s quark contributions, $G_E^s(Q^2)$ and $G_M^s(Q^2)$, to the overall charge and magnetization densities of the nucleon using these measurements. No other existing or proposed experiment will perform the separation over this range of momentum transfers. At backward angles we will measure quasi-elastic scattering from a deuterium target to extract the nucleon anapole form factor (sometimes referred to as "radiative correction") contributions (included in $G_A^e(T=1)$) to these asymmetries. Although the SAMPLE experiment has shown that this contribution is in agreement with the prediction at zero momentum transfer, there are essentially no predictions of the momentum transfer dependence in the range of the G0 experiment. In Table 1.1 we show the impact of the uncertainty in G_A^e on the determination of G_E^s and G_M^s. In the case of G_M^s, it is clear that any uncertainty in G_A^e larger than the *estimated* theoretical uncertainty at $Q^2 = 0$ (such as, for example, the uncertainty in the two SAMPLE measurements) will dominate its overall uncertainty (see also Section 6.1). We therefore believe it is imperative to measure the deuterium quasi-elastic asymmetries to determine this quantity experimentally (see also Section 2.2 and especially Figure 2.3). *The backward angle measurements proposed herein, in combination with the forward angle measurement just completed, are necessary to separate these three form factors.*

Furthermore, we believe we can make a substantially better measurement because we have shown that our target (and detectors) can run comfortably at 80 μA for the backward angle run. In the previous proposal, fully 1/2 (3/4) of the contributions to the quadrature sum uncertainties for G_M^s (G_A^e) were due to backward angle statistical precision. In keeping with the philosophy of making as precise a determination of these form factors as reasonable in the G0 experiment, we think it is important to the physics to take advantage of this extra factor in the uncertainty. We are therefore requesting the same amount of beam time with the added beam current.

Q^2	dG_E^s/dG_A^e	dG_M^s/dG_A^e
0.3	0.063	0.313
0.5	0.077	0.245
0.8	0.093	0.197

Table 1.1: Derivatives of the extracted G_E^s and G_M^s with respect to G_A^e for the case of a hydrogen-only back angle measurement. In such a situation, the relatively unknown value of G_A^e at these momentum transfers will dominate the uncertainties of G_M^s in particular.

A special purpose, superconducting toroidal spectrometer with large, azimuthally symmetric angular acceptance and an associated cryogenic target have been constructed for these measurements. Over the past 18 months, this equipment has been commissioned and used by the G0 collaboration (see Table 1.2 for a current collaboration list) to complete the forward angle measurement. A summary of the results of the *commissioning* runs, reported to the laboratory in March 2004, is included in Appendix A. It includes demonstration of the key performance issues in the experiment from statistical precision, to control of false asymmetries arising from helicity-correlated beam properties and experimental effects.

Recent examples of the data quality in the forward angle *production* measurement are presented in Figures 1.1 and 1.2.* These preliminary figures demonstrate that the false asymmetries as measured by the luminosity monitors are small (< 0.1 ppm) on the scale of the smallest physics asymmetries (~ 3 ppm). The detector asymmetries are shown in Fig. 1.2 for four regions of our t.o.f. spectra, where the appropriate reversal of the asymmetry with "$\lambda/2$ waveplate insertion"† is demonstrated in that the asymmetry sum for the two states is consistent with zero for all regions. These results are shown for the period where G0 ran with only Hall B; a false asymmetry related to "leakage" beam currents was discovered during running with Halls A and B together. A summary of the tests performed and corrections required is presented in Appendix B. *It is important to note that this false asymmetry will not affect the backward angle experiment as it will be run with the same beam structure – 499 MHz – as the other halls* (see also below).

Detection of electrons in the backward angle experiment requires a new set of scintillator detectors to be placed near the spectrometer exit windows (see Section 4.1.2). Running with a deuterium target necessitates particle identification measurements for which we propose adding a Cherenkov counter, to be discussed in detail in Sections 3.3 and 4.1.3. Otherwise, especially in terms of the standard false asymmetries, the forward and backward angle measurements are essentially the same (asymmetries are larger in the backward direction). At the backward angles we will also measure the axial vector N-Δ transition form factor (a separate proposal has been submitted for this experiment; the relevant technical sections of the two proposals are the same).

*It is important to note that the luminosity monitors integrate all events and are therefore not susceptible to the leakage current effects. To the extent that the leakage current effects reverse with $\lambda/2$ waveplate setting, they are absent from the IN+OUT spectra as well.

†Slow helicity reversal is effected by inserting a $\lambda/2$ waveplate in the polarized source laser beam – reversing the helicity of the electrons at the target

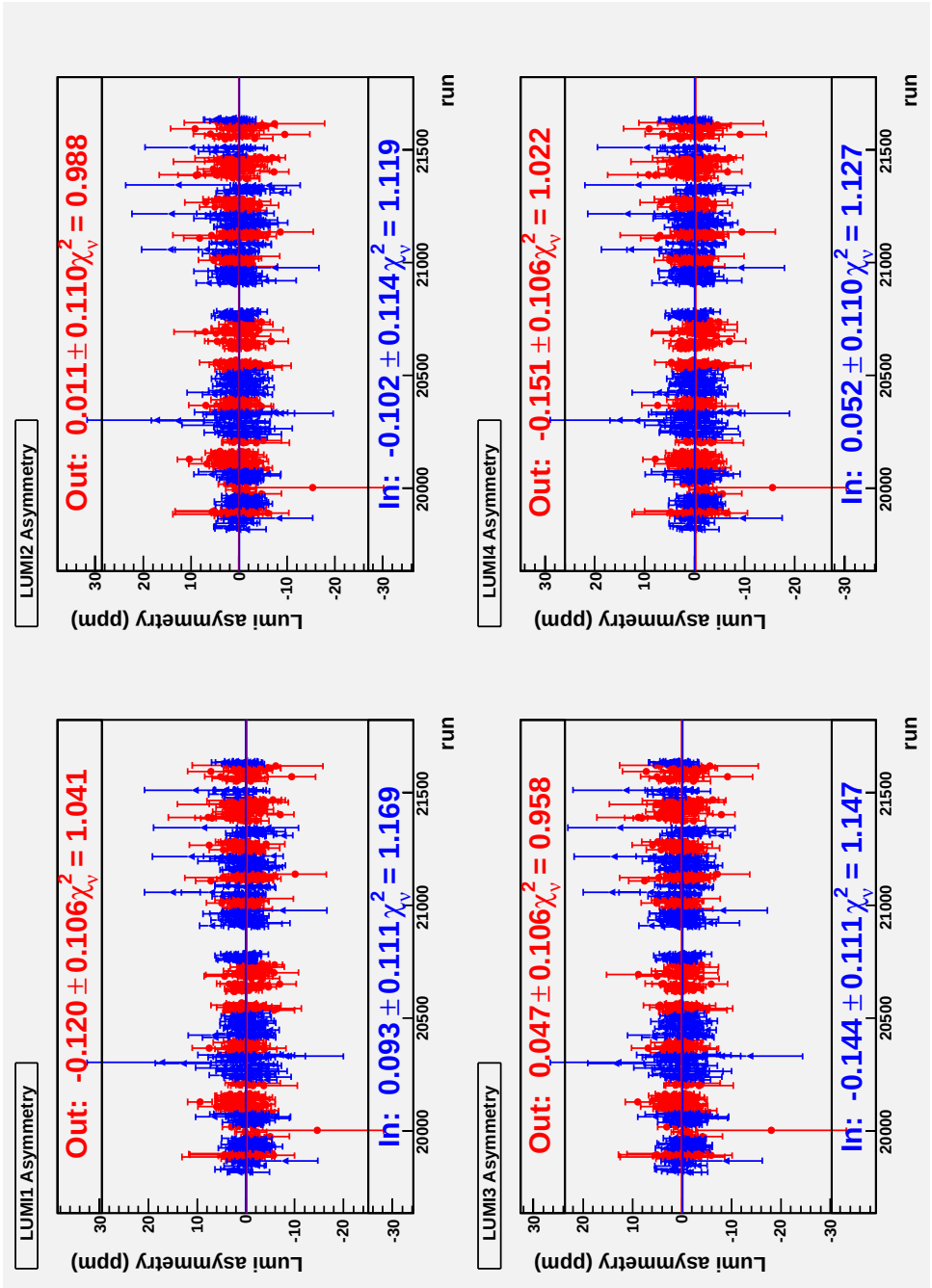

Figure 1.1: Asymmetries measured with the small angle luminosity monitors in the G0 forward angle experiment. The physics asymmetries for these detectors are expected to be < 0.1 ppm.

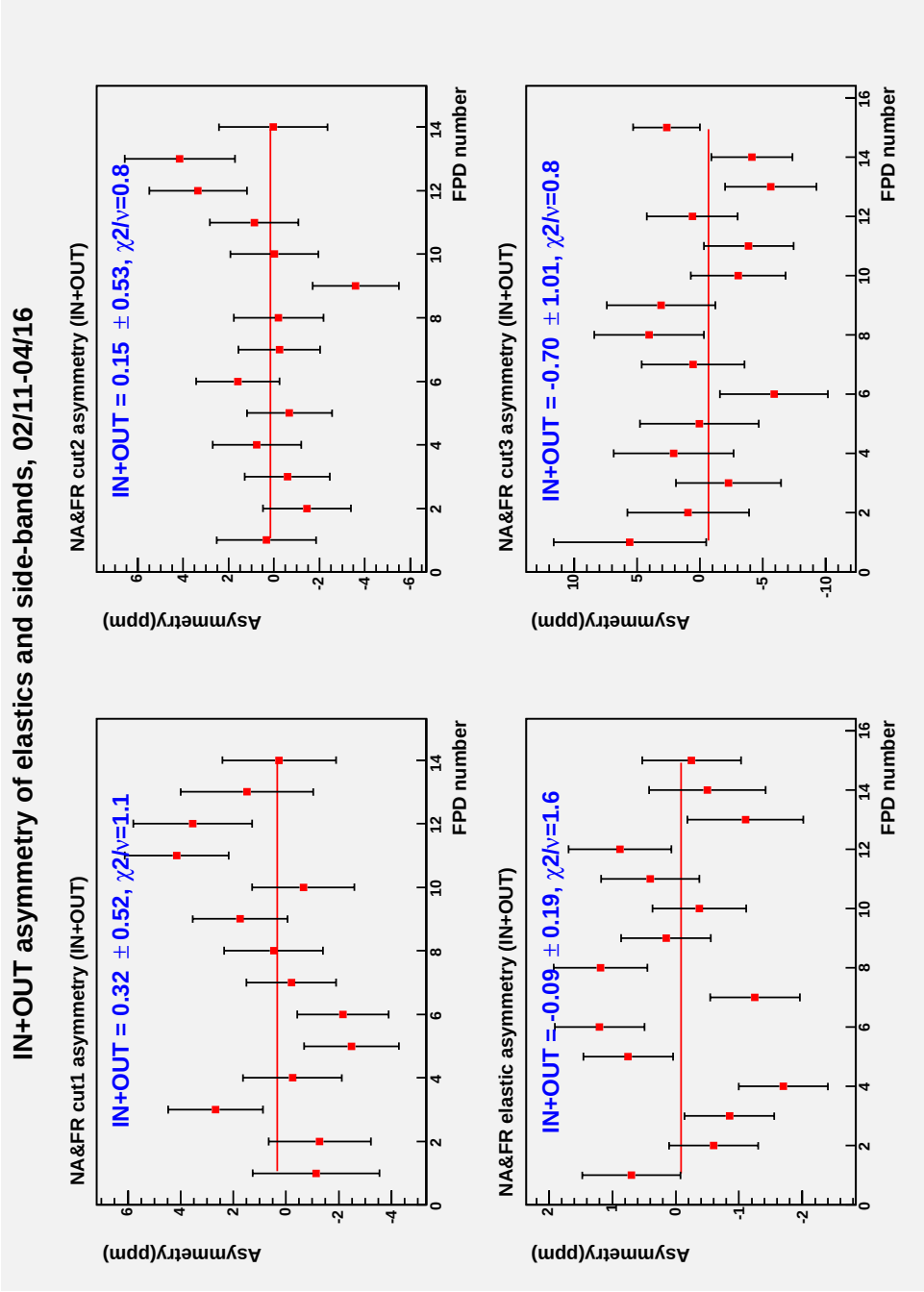

Figure 1.2: Examples of the sum of asymmetries for the two $\lambda/2$ waveplate states ("IN" and "OUT") for part of the forward angle dataset. The four panels show these sums for the four time-of-flight (t.o.f) regions of interest: cuts 1 and 2 (3) represent yield at shorter (longer) t.o.f. than the elastic. The data are plotted as a function of detector number – corresponding to increasing Q^2.

A few of the lessons learned in the course of the forward running have changed our plans for the backward angle running. Most importantly, we have concluded that there are significant practical and experimental advantages to running with a standard 499 MHz bunch structure, rather than the 31 MHz structure used for the forward angle measurement. Because the backward angle experiment does not require t.o.f., we have modified our plan for the electronics to use a standard trigger generated by our detectors, rather than using the beam pickoff method used for the forward running. This will allow us to use the 499 MHz structure and still have less deadtime than the forward measurement (the rates in the backward measurement are much lower). In addition, we expect that use of the 499 MHz structure will allow us to run higher beam currents and reduce the statistical uncertainty in the back angle measurements that dominate our overall uncertainty in extraction of G_E^s, G_M^s and G_A^e. Based on the target boiling and overall cooling power studies performed during the forward measurement, we expect to be able to run with a beam current of at least 80 μA. We are also currently investigating the cost of a "load-lock" system for the target, which would allow us to repair the target in case of failure without warming up the magnet (as is currently the case), thereby providing additional insurance for completing runs.

A first measurement at backward angles was conditionally approved by PAC 20, with the comments

> "In addition, after discussions with Associate Director, Larry Cardman, the backward angle G0 measurement (E-01-116), which will follow the planned forward angle running, was conditionally approved for 60 days (with E-01-115 running in parallel) but was treated as outside the immediate Hall C allocation. Conditional approval of at least some backward angle running for G0 has been implicit in previous PAC discussions of this major research program."
>
> "Conditional approval for 60 days in Hall C, depending on demonstrated performance of the necessary components."

With this submission, we again propose that the backward angle measurements of the G0 experiment include three momentum transfers (Q^2 = 0.3, 0.5 and 0.8 GeV^2) to provide reasonable information on the Q^2 dependence of G_E^s, G_M^s and $G_A^e(T=1)$ within the range accessible to the experiment. The choice of which Q^2 value to run will be driven by the physics outcome of the forward angle measurement (running completed May 17, 2004) and will be made in consultation with the lab. At this time we therefore request the PAC to

- re-approve the 60 beam days (30 d each for measurements with hydrogen and deuterium targets) conditionally approved for the first backward angle measurement,
- re-consider the 10 days of commissioning time prior to the first backward angle measurement in support of testing the new detectors (cryostat exit and Cherenkov) and electronics

The commissioning of the new detectors (CED and Cherenkov), electronics, and background and target configurations will follow the outline of the successfull commissioning of the existing equipment (45 days) with roughly six shifts for each activity interspersed

R. D. McKeown[†]				
Carnegie-Mellon University				
A. Biselli	G. Franklin	J. Kuhn	J. Lachniet[f]	B. Quinn[†]
College of William and Mary				
D. S. Armstrong[†]	T. D. Averett	S. Bailey	J. M. Finn	K. A. Griffioen
K. Grimm	B. Moffit	S. Phillips[f]	J. Secrest[f]	A. Slaughter[f]
V. Sulkosky[f]				
IPN Orsay				
J. Arvieux[†]	L. Bimbot	E. Boukobza	H. Guler[*]	J. Lenoble
B. Loupias	D. Marchand	M. Morlet[f *]	J. van de Wiele	
LPSC Grenoble				
G. Batigne[f *]	C. Furget	B. Guillon[f]	S. Kox[†]	E. Liatard[f *]
F. Merchez[f *]	G. Quemener[f]	J. Real	R. Tieulent[f *]	E. Voutier
Louisiana Tech. Univ.				
T. A. Forest	K. Johnston	J. S. Kraft	M. Novovic[f]	N. Simicevic
S. Wells[†]				
New Mexico State University				
G. MacLachlan	D. McKee	V. Papavassiliou[†]	S. Pate[†]	A. W. Rauf[f]
TJNAF				
J. Beaufait	R. D. Carlini	Y. Chao[*]	S. Chattopadhyay[*]	D. Gaskell
J. Grames[*]	J. Hansknecht[*]	M. Jones	R. Kazimi[*]	A. Lung
M. Poelker[*]	J. Roche	G. Smith[†]	W. F. Vulcan	G. Warren
S. A. Wood				
TRIUMF				
C. A. Davis[†]				
University of Connecticut				
M. J. Ramsey-Musolf[†*]				
University of Illinois				
D. H. Beck[†]	P. Kammel	P. M. King	M. Muether[b]	K. Nakahara[f]
R. Neveling[f]	D. T. Spayde	S. Williamson[†]		
University of Kentucky				
D. Dale	A. Kolarkar	W. Korsch[†]	I. Nakagawa	
University of Manitoba				
J. Birchall	W. R. Falk	Z. Ke	L. Lee	S. A. Page
W. D. Ramsay	G. A. Rutledge	M. Steeds[b]	W. T. H. van Oers[†]	
University of Maryland				
E. J. Beise[†]	H. Breuer	T. Horn	J. Liu[f]	P. Roos
University of Massachusetts				
B. R. Holstein[†*]				
University of Northern British Columbia				
E. Korkmaz[†]	T. Porcelli			
Virginia Tech				
M. L. Pitt[†]	J. Yun[f]			
Yerevan Physics Institute				
R. Asaturyan	H. Mkrtchyan[†]	T. Navasardyan	V. Tadevosyan	

Table 1.2: Active participants in the G^0 collaboration († indicates a contact person, $*$ indicates one who does not take shifts, f indicates participation in forward angle measurements only, b indicates participation in backward angle measurements only).

throughout the commissioning period. We note that the time requested here for the back angle running is based on a rough equalization of contributions from the forward and backward angle asymmetries to the overall uncertainty in the form factors (see Section 6.1). Increased beam current will provide better measurements of all three form factors, but particularly for G_M^s and G_A^e in the same amount of beam time.

In this proposal we present a discussion of the back angle elastic scattering experiment, descriptions of the target, detectors and electronics to be used and conclude with a discussion of status, planning and the beam time request.

2 Physics

The parity-violating interaction between electrons and nucleons primarily involves interference between the dominant electromagnetic (γ exchange) and the exchange of a Z boson. Due to the parity-violating nature of the weak interaction, these interference effects imply the existence of small pseudoscalar observables in electron scattering experiments. Much of the discussion in this section is elaborated upon in the review article [1] by D. Beck and R. McKeown.

One generally measures the ratio of helicity dependent to helicity independent cross sections, or the parity-violating asymmetry:

$$A = \frac{d\sigma_R - d\sigma_L}{d\sigma_R + d\sigma_L} \tag{2.1}$$

where σ_R and σ_L are the cross sections for right- and left-handed electrons, respectively. This quantity will be proportional to a product of neutral weak couplings $v^Z \cdot a^Z$ that contains the physics of interest. Thus, measurement of the helicity dependence in elastic electron-proton scattering can be used to study the neutral weak vector form factors of the nucleon [2, 3, 4]. There is also sensitivity to the weak axial vector form factors; these are suppressed at leading order but are also of great interest and should be measured.

The parity-violating asymmetry for elastic electron-proton scattering is given by the following expression [5]:

$$A = \left[\frac{-G_F Q^2}{4\sqrt{2}\pi\alpha}\right] \frac{\varepsilon G_E^\gamma G_E^Z + \tau G_M^\gamma G_M^Z - (1 - 4\sin^2\theta_W)\varepsilon' G_M^\gamma G_A^e}{\varepsilon (G_E^\gamma)^2 + \tau (G_M)^2} \tag{2.2}$$

$$\equiv -\frac{G_F Q^2}{4\sqrt{2}\pi\alpha} \times \frac{\mathcal{N}}{\mathcal{D}} \tag{2.3}$$

where

$$\begin{aligned} \tau &= \frac{Q^2}{4M_N^2} \\ \varepsilon &= \frac{1}{1 + 2(1+\tau)\tan^2\frac{\theta}{2}} \\ \varepsilon' &= \sqrt{\tau(1+\tau)(1-\varepsilon^2)} \end{aligned} \tag{2.4}$$

are kinematic quantities, $Q^2 > 0$ is the four-momentum transfer, and θ is the laboratory electron scattering angle.

The quantities G_E^γ, G_M^γ, G_E^Z, and G_M^Z are the vector form factors of the nucleon associated with γ- and Z-exchange. The electromagnetic and weak form factors are (in lowest order) related via the flavor dependence of the fundamental Z-q couplings. The flavor structure of these form factors and the radiative corrections are considered in more detail below.

The neutral weak e-N interaction also involves an axial vector coupling G_A^e in the third term of the numerator in Eqn.(2.2). The tree-level Z-exchange process is responsible for the $1-4\sin^2\theta_W$ factor (proportional to the neutral weak *vector* charge of the electron) that appears in this expression and, as noted in [5, 6], higher order processes can contribute significantly. These include interesting anapole effects and other electroweak radiative corrections as discussed below.

It is important to note that the three terms in the numerator can be separately determined via a series of measurements. At very small scattering angles (and low momentum transfer), the G_E term has its maximum contribution due to the large value of ϵ. This is the focus of the recently completed G0 forward angle measurements. At larger scattering angles, one is sensitive to a combination of both the G_M^Z term and the G_A^e (axial) term. Although one expects the G_M^Z term to be dominant, the axial term can not be neglected, and indeed it is of great interest to study this term as well. Separation of these terms via kinematic measurements on the proton is extremely difficult. The best method to separate the magnetic and axial terms is to utilize quasielastic scattering from deuterium.

For a nucleus with Z protons and N neutrons the quasielastic asymmetry can be written in the simple form (ignoring final state interactions and other nuclear corrections):

$$A_{\rm nuc} = -\frac{G_F Q^2}{4\sqrt{2}\pi\alpha} \times \frac{N\mathcal{N}_n + Z\mathcal{N}_p}{N\mathcal{D}_n + Z\mathcal{D}_p} \tag{2.5}$$

where $\mathcal{N}_p$ ($\mathcal{N}_n$) is the numerator expression and $\mathcal{D}_p$ ($\mathcal{D}_n$) the denominator (from Eqns. 2.2 and 2.3) for the proton (neutron), respectively. Effects associated with the deuteron wavefunction and different potential models have been explored in [7] and shown to be quite small. Of course, the corrections for final state interactions and exchange currents must be made to enable reliable separation of the axial and magnetic form factors and the theory of these effects is now thought to be under control. These issues have been addressed in recent work by Diaconescu, *et al.*[8] and Liu, *et al.*[9]. Experimental validation has been provided by the SAMPLE experiment in deuterium measurements at two low values of momentum transfer [10].

In order to determine G_E^s, G_M^s, and G_A^e it is necessary to perform at least 3 independent measurements at each Q^2. The G0 program is a unique opportunity to perform a series of such measurements: the forward angle measurement on the proton, a backward angle measurement on the proton, and also a backward angle measurement of the quasielastic deuteron asymmetry.

2.1 Nucleon Vector Form Factors and Strangeness Content

The standard electroweak model couplings to the up, down, and strange quarks imply that the electromagnetic current operator has the simple familiar form

$$\hat{V}_\gamma^\mu = \frac{2}{3}\bar{u}\gamma^\mu u - \frac{1}{3}\bar{d}\gamma^\mu d - \frac{1}{3}\bar{s}\gamma^\mu s\,. \tag{2.6}$$

Similarly, the neutral weak vector current operator is given by the expression

$$\hat{V}_Z^\mu = (1 - \frac{8}{3}\sin^2\theta_W)\bar{u}\gamma^\mu u + (-1 + \frac{4}{3}\sin^2\theta_W)\bar{d}\gamma^\mu d + (-1 + \frac{4}{3}\sin^2\theta_W)\bar{s}\gamma^\mu s\,. \qquad (2.7)$$

Here the coefficients depend on the weak mixing angle, which is very accurately known ($\sin^2\theta_W = 0.23117 \pm 0.00016$ [11]). The flavor structure contained in these expressions forms the basis for a program to measure the flavor composition of the vector form factors. The measurements involve matrix elements of these operators (the form factors) which will reflect their underlying flavor dependence.

The electromagnetic form factors of the nucleon arise from matrix elements of the EM current operator

$$< N|\hat{V}_\gamma^\mu|N > \equiv\ \bar{u}_N\Big[F_1^\gamma(q^2)\gamma^\mu + \frac{i}{2M_N}F_2^\gamma(q^2)\sigma^{\mu\nu}q_\nu\Big]u_N \qquad (2.8)$$

where $F_1^\gamma(q^2)$ and $F_2^\gamma(q^2)$ are the Dirac and Pauli electromagnetic form factors, which are functions of the squared momentum transfer. We will also use the Sachs form factors, which are linear combinations of the Dirac and Pauli form factors

$$\begin{aligned} G_E &= F_1 - \tau F_2 \\ G_M &= F_1 + F_2 \end{aligned} \qquad (2.9)$$

where $\tau \equiv -q^2/4M_N^2 > 0$.

The quark flavor structure of these form factors can be revealed by writing the matrix elements of individual quark currents in terms of form factors:

$$< N|\bar{q}^j\gamma^\mu q^j|N > \equiv\ \bar{u}_N\Big[F_1^j(q^2)\gamma^\mu + \frac{i}{2M_N}F_2^j(q^2)\sigma^{\mu\nu}q_\nu\Big]u_N \qquad (2.10)$$

where $j = u, d$, or s; this defines the form factors F_1^j and F_2^j. Then using definitions analogous to Eqn. (2.9), we can write

$$G_E^\gamma = \frac{2}{3}G_E^u - \frac{1}{3}G_E^d - \frac{1}{3}G_E^s \qquad (2.11)$$

$$G_M^\gamma = \frac{2}{3}G_M^u - \frac{1}{3}G_M^d - \frac{1}{3}G_M^s\,. \qquad (2.12)$$

In direct analogy to Eqn. (2.7), we have expressions for the neutral weak form factors G_E^Z and G_M^Z in terms of the different quark flavor components:

$$G_{E,M}^Z = (1 - \frac{8}{3}\sin^2\theta_W)G_{E,M}^u + (-1 + \frac{4}{3}\sin^2\theta_W)G_{E,M}^d + (-1 + \frac{4}{3}\sin^2\theta_W)G_{E,M}^s\,. \qquad (2.13)$$

Again it is important to emphasize that the form factors $G_{E,M}^{u,d,s}$ appearing in this expression are *exactly* the same as those in the electromagnetic form factors in Eqns. (2.11, 2.12).

Utilizing charge symmetry, one then can eliminate the up and down quark contributions to the neutral weak form factors using the proton and neutron electromagnetic form factors and obtain the expressions

$$G_{E,M}^{Z,p} = (1 - 4\sin^2\theta_W)G_{E,M}^{\gamma,p} - G_{E,M}^{\gamma,n} - G_{E,M}^{s} \ . \tag{2.14}$$

This is a key result. It shows how the neutral weak form factors are related to the electromagnetic form factors plus a contribution from the strange (electric or magnetic) form factor. Thus measurement of the neutral weak form factor will allow (after combination with the electromagnetic form factors) determination of the strange form factor of interest.

The electromagnetic form factors present in Eqns. (2.11,2.12) are very accurately known (1-2 %) for the proton in the momentum transfer region $Q^2 < 1$ (GeV/c)^2. The neutron form factors are not known as accurately as the proton form factors, but a good deal of progress has been made recently and more experimental results are expected soon [12]. The improving knowledge of the neutron form factors will not significantly hinder the interpretation of the neutral weak form factors.

In obtaining Eqn. (2.14), it was assumed that charge symmetry was exact. Electromagnetic and quark mass effects can cause small violations of charge symmetry and introduce corrections to this relation. The effects of charge symmetry violation on the extraction of strange form factors from neutral weak and electromagnetic form factors has been treated in some detail in [13]. In that work it is found that these corrections are very small, generally less that about 1% of the electromagnetic form factors, and have only a minor effect the extraction of the strange form factors.

As mentioned above, there are electroweak radiative corrections to the coefficients in Eqn. (2.14) due to processes such as those shown in Figure 2.1. The above expressions for the neutral weak vector form factors $G_{p,n}^{Z}$ in terms of the electromagnetic form factors $G_{p,n}^{\gamma}$ are modified according to

$$G_{E,M}^{Z,p} = (1 - 4\sin^2\theta_W)(1 + R_V^p)G_{E,M}^{\gamma,p} - (1 + R_V^n)G_{E,M}^{\gamma,n} - G_{E,M}^{s} \ . \tag{2.15}$$

The correction factors have been computed [14, 6, 5] to be

$$\begin{aligned} R_V^p &= -0.054 \pm 0.033 \\ R_V^n &= -0.0143 \pm 0.0004. \end{aligned} \tag{2.16}$$

The properties of the strange form factors G_E^s and G_M^s near $Q^2 = 0$ are of particular interest in that they represent static properties of the nucleon. Thus it is customary to define the quantity

$$\mu_s \equiv G_M^s(Q^2 = 0) \tag{2.17}$$

as the strange magnetic moment of the nucleon. Since the nucleon has no net strangeness, we find $G_E^s(Q^2 = 0) = 0$. However, one can express the slope of G_E^s at $Q^2 = 0$ in the usual fashion in terms of a "strangeness radius" r_s

$$r_s^2 \equiv -6\left[dG_E^s/dQ^2\right]_{Q^2=0} \ . \tag{2.18}$$

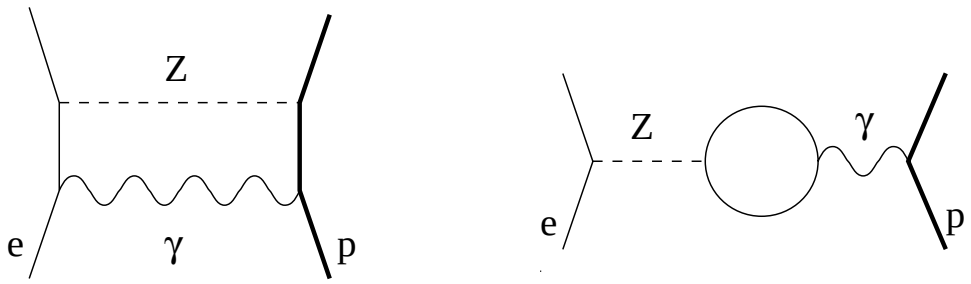

Figure 2.1: Examples of amplitudes contributing to electroweak radiative corrections ("$\gamma - Z$ box" on the left) and anapole corrections ("$\gamma - Z$ mixing" on the right).

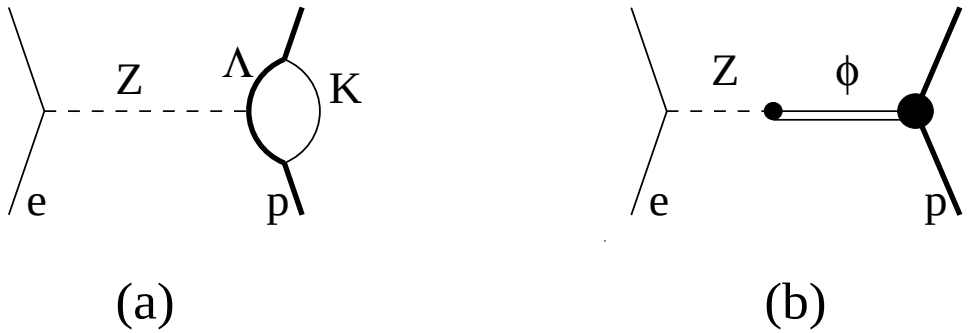

Figure 2.2: Examples of (a) loop and (b) pole diagrams used to compute strangeness effects in the nucleon.

A variety of theoretical methods have been employed in efforts to compute the form factors $G^s_{E,M}(Q^2)$ (or often just the quantities μ_s and r_s). Figure 2.2 shows two examples of physical processes that may contribute. These are generically known as "loop" effects and "pole" effects. The loop effects [15, 16, 17, 18, 19] correspond to the fluctuation of the nucleon into a K-meson and hyperon. The physical separation of the s and $\bar{s}$ in such processes (or the production of $s\bar{s}$ in a spin singlet) leads to non-zero values of $G^s_{E,M}(Q^2)$. The pole processes [21, 22, 23] are associated with the fluctuation of the virtual boson (photon or Z) into a ϕ meson, which is predominantly an $\bar{s}s$ pair. Some attempts have been made to combine the two approaches using dispersion theoretical analyses [24]. Other models employ SU(3) extensions of the Skyrme model [25, 26, 27, 28] or the Nambu-Jona-Lasinio model. [32] Excited hyperons and strange mesons are also included in some treatments, and these contributions seem to be numerically significant. [19, 20] A detailed review of the various calculations can be found in Ref. [33].

A reasonably complete compilation of theoretical results for μ_s and r_s^2 is listed in Table 2.1. The calculated values of r_s^2 are small and there is no general agreement on the sign. However, there is evidently a trend in Table 2.1 that one should expect $\mu_s < 0$, generally in the range $-0.8 \rightarrow 0.0$ nuclear magnetons. Notable exceptions are references [26] and [28] which analyze the set of baryon magnetic moments in the context of a SU(3) generalization of the Skyrme model Hamiltonian.

Table 2.1: Theoretical predictions for $\mu_s \equiv G_M^s(Q^2=0)$ and r_s^2.

Type of calculation	μ_s (n.m.)	r_s^2(fm^2)	Reference
Poles	-0.31 ± 0.09	$0.11 \to 0.22$	[21]
Kaon Loops	$-0.31 \to -0.40$	$-0.032 \to -0.027$	[15]
Kaon Loops	-0.026	-0.01	[16]
Kaon Loops	$\lvert\mu_s\rvert = 0.8$		[17]
SU(3) Skyrme (broken)	-0.13	-0.10	[25]
SU(3) Skyrme (symmetric)	-0.33	-0.19	[25]
SU(3) chiral hyperbag	$+0.42$		[26]
SU(3) chiral color dielectric	$-0.20 \to -0.026$	-0.003 ± 0.002	[34]
SU(3) chiral soliton	-0.45	-0.35	[27]
Poles	-0.24 ± 0.03	0.19 ± 0.03	[22]
Kaon Loops	$-0.125 \to -0.146$	$-0.022 \to -0.019$	[18]
NJL soliton	$-0.05 \to +0.25$	$-0.25 \to -0.15$	[32]
QCD equalities	-0.75 ± 0.30		[35]
Loops	$+0.035$	-0.04	[19]
Loops	-0.06	$+0.02$	[20]
Dispersion	$-0.10 \to -0.14$	$0.21 \to 0.27$	[24]
Chiral models	$-0.25, -0.09$	0.24	[36]
Poles	0.003	0.002	[23]
SU(3) Skyrme (broken)	$+0.36$		[28]
Lattice (quenched)	-0.36 ± 0.20	$-0.06 \to -0.16$	[29]
Lattice (chiral)	-0.16 ± 0.18		[30]
Lattice (octet)	-0.051 ± 0.021		[31]

2.2 Anapole form factor

As noted above, the parity-violating interaction of electrons with nucleons involves an axial vector coupling to the nucleon, G_A^e. This term in the parity-violating asymmetry contains several effects beyond the leading order Z- exchange which can only be differentiated in theoretical calculations (if at all). Nevertheless, it is important to establish that the *experimentally observable* quantities are well-defined and unambiguous.

In parity-violating electron scattering the neutral weak axial form factor corresponding to tree-level Z-exchange is multiplied by the coefficient $1 - 4\sin^2\theta_W \ll 1$. This suppression of the leading amplitude increases the importance of anapole effects and other electroweak radiative corrections

$$G_A^e = G_A^Z + \eta F_A + R_e \tag{2.19}$$

where

$$\eta = \frac{8\pi\sqrt{2}\alpha}{1 - 4\sin^2\theta_W} = 3.45, \tag{2.20}$$

$G_A^Z = G_A\tau_3 + \Delta s$, F_A is the nucleon anapole form factor (defined below), and R_e are radiative corrections. The normalization of $G_A\tau_3$ is obtained from neutron beta decay and its Q^2 dependence from charged current neutrino scattering; Δs is estimated from spin

dependent deep inelastic scattering. G_A^Z is therefore completely determined by experiments independent of the present one. Typical contributions to R_e and F_A are shown in Figure 2.1. As discussed in [5, 6], the separation of F_A and R_e is actually a theoretical issue and dependent upon the choice of gauge. In calculations performed to date [14, 37] the anapole type effects associated with the "$\gamma - Z$ mixing" amplitudes are, in fact, the dominant correction. We thus refer to the observable difference between G_A^e and G_A^Z as an anapole contribution, with the caveat that the complete set of radiative corrections must be included in any consistent quantitative theoretical treatment of G_A^e.

The anapole moment has been traditionally defined as the effective parity-violating coupling between real photons and nucleons [38]. (In practice, this quantity is only observable at finite momentum transfer associated with the parity-violating interaction between electrons and nucleons.) It appears as an additional term in Eqn. (2.8) when one includes the possibility that parity is not strictly conserved [37]:

$$\begin{aligned} \langle N|\hat{V}_\gamma^\mu|N\rangle &\equiv \bar{u}_N(p')\{F_1\gamma^\mu + \frac{i}{2M_N}F_2\sigma^{\mu\nu}q_\nu \\ &+ F_A\left[G_F(q^2\gamma^\mu - q^\nu\gamma_\nu q^\mu)\gamma^5\right]\}u(p) \end{aligned} \tag{2.21}$$

Note that our definition of F_A differs from that used in the atomic physics literature by a factor of $M_N^2 G_F$ with the result that the natural scale of F_A is of order unity. Thus, F_A could indeed provide a substantial contribution to G_A^e (see Eqn. (2.19)).

As mentioned above, aside from the leading Z exchange term (G_A^Z), the dominant calculated contribution to G_A^e arises from the "$\gamma - Z$ mixing" diagram shown in Figure 2.1 [14, 37]. It should be noted that the evaluation of this amplitude ignores the strong interaction of the nucleon with the quark loop and so may not be numerically accurate. More recently, consideration of additional strong interaction effects associated with mesonic processes have indicated only relatively small additional corrections [41, 42, 43, 44]. It is important to note that the Q^2 dependence of the anapole form factor F_A could be different from the dipole form that is successful in fitting the tree level term G_A^Z. Maekawa and van Kolck [43] find to leading order in chiral perturbation theory that the momentum dependence of at least the isoscalar piece of the anapole form factor is softer than the dipole form (corresponding to a small radius for the anapole distribution); in this framework the isovector anapole moment is zero in leading order. In Figure 2.3, we present the difference between $G_A^e(Q^2)$, the axial form factor measured in PV electron scattering, and $G_A(Q^2)$, the corresponding quantity for neutrino scattering; the expected precision of the G0 measurements is also shown. As can be seen the combination of the $Q^2 = 0$ calculation and the SAMPLE data provide no real information about this difference in the Q^2 range of the proposed G0 separation. The study of the anapole contributions and other corrections to G_A^e is presently an active area of experimental and theoretical investigation and it is important to measure this quantity over a range of Q^2 values. [43]

2.3 Other experiments: past and future

The SAMPLE experiment at the Bates Linear Accelerator Center was the first to study strange form factors and the anapole contribution in parity-violating electron scattering.

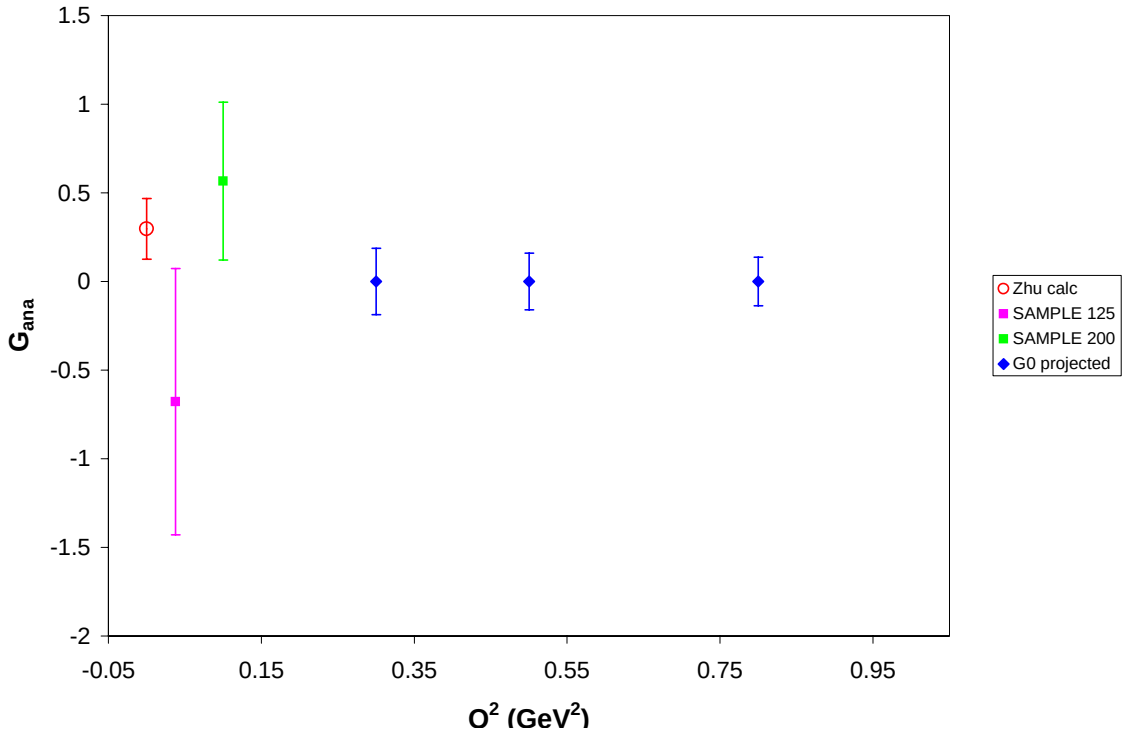

Figure 2.3: Compilation of the theoretical and experimental information on the difference between $G_A^e(T=1)$ as measured in PV electron scattering and G_A from neutrino scattering. At present there is no theoretical calculation of the momentum transfer dependence of $G_A^e(T=1)$.

This experiment measures the elastic asymmetry from the proton and the quasielastic asymmetry from the deuteron at $Q^2 = 0.1$ GeV^2 [45, 46, 47, 48, 49]. In the most recent publication [50], analysis of the SAMPLE results is presented which yields a value of the strange quark contribution to the magnetic form factor

$$G_M^s(Q^2 = 0.1) \quad = \quad +0.37 \pm 0.20 \pm 0.26 \pm 0.07\,, \tag{2.22}$$

where the last uncertainty is due to uncertainties in the radiative corrections. The result for G_M^s is somewhat surprising, as its value was generally expected to be negative, based on the theoretical calculations (see Table 2.1). The values for G_A^e at both low momentum transfers measured in the experiment ($Q^2 \sim 0.03, 0.10$ GeV^2) are consistent [10] with the theoretical expectation of $G_A^e(T=1) = -0.83 \pm 0.26$ [41]. As noted above, the Q^2 dependence of G_A^e is not easily calculated but there are indications that the it is softer than a dipole form [43]. It is essential at the higher momentum transfers of interest here to measure the axial form factor to extract reliable values of G_M^s, and of course G_A^e itself is quite interesting to study experimentally.

The HAPPEX experiment [53, 54] utilized the two spectrometers in Hall A at Jefferson Lab to measure parity violation in elastic electron scattering at very forward angles. The measured asymmetry, including the results from both phases of the experiment is

$$A_p(Q^2 = 0.477\text{GeV}^2,\, \theta_{av} = 12.3^\circ) = -14.60 \pm 0.94 \pm 0.54 \text{ ppm}\,. \tag{2.23}$$

This result has been interpreted (using an assumed value of G_A^e extrapolated from calculated $Q^2 = 0$ values) to yield the strange form factor combination

$$\frac{G_E^s + 0.392 G_M^s}{G_M^p/\mu_p} = 0.091 \pm 0.054 \pm 0.039 \; . \tag{2.24}$$

While the results of the HAPPEX experiment exhibit small statistical uncertainties, it is difficult to draw firm conclusions about the form factors from this single measurement.

The first PVA4 measurement [55] also determined a combination of form factors at a forward angle using an array of PbF_2 detectors. They measure

$$A_p(Q^2 = 0.230 \mathrm{GeV}^2, \, \theta_{av} = 35.3^\circ) = -5.44 \pm 0.54 \pm 0.26 \text{ ppm} \, , \tag{2.25}$$

as compared with the expectation $A_0 = -6.30 \pm 0.43$ ppm, again using an extrapolation of G_A^e from zero momentum transfer and zero strange quark contribution. With the same approximation for G_A^e they obtain

$$G_E^s + 0.225 G_M^s = 0.039 \pm 0.035. \tag{2.26}$$

With some assumptions about G_M^s they further determine

$$G_E^s \left(Q^2 = 0.23 \text{ GeV}^2 \right) = 0.061 \pm 0.035 \tag{2.27}$$

and further that

$$G_E^s \left(0.1 \leq Q^2 \leq 0.5 \text{ GeV}^2 \right) = 0.066 \pm 0.026 \tag{2.28}$$

when combined with the HAPPEX results. Similar information is contained in the summary graph presented in Figure 2.4.

Several future measurements are planned. The HAPPEX collaboration is presently measuring the forward angle asymmetry at $Q^2 = 0.11$ GeV^2 for both proton and ^{4}He targets. The proton measurement will provide information just below the range of the G0 experiment and complementary to the SAMPLE backward angle experiment; the ^{4}He measurement is sensitive to only G_E^s and not G_M^s or G_A^e (because it is a 0^{++} nucleus) and will therefore provide a cross check. In Mainz, data have already been taken at 570 MeV ($Q^2 = 0.11$ GeV^2) on a proton target and analysis is underway. There are also definite plans to run PVA4 with a deuterium target *at forward angles* with 855 and 570 MeV incident energy beams. It is also possible to rotate the PVA4 apparatus and measure at backward angles, although there are no definite plans to do so at the moment. Therefore, the G0 experiment remains the only one where an experimental determination of the three form factors over the range of momentum transfers from about 0.1 to 1 GeV^2 is planned.

In summary, if there is evidence for the presence of strange quark contributions in the data obtained so far, interpretation is hindered by the dependence of the measured forward asymmetries on three form factors. Particularly for the HAPPEX kinematics, theory offers little guidance about these form factors or their inter-relationships. Therefore, it is crucial to perform the backward angle G0 measurements on proton and deuteron targets to complement the existing G0 forward angle data and ultimately enable a clear and unambiguous interpretation in terms of nucleon form factors with the best possible precision over a wide range of momentum transfers.

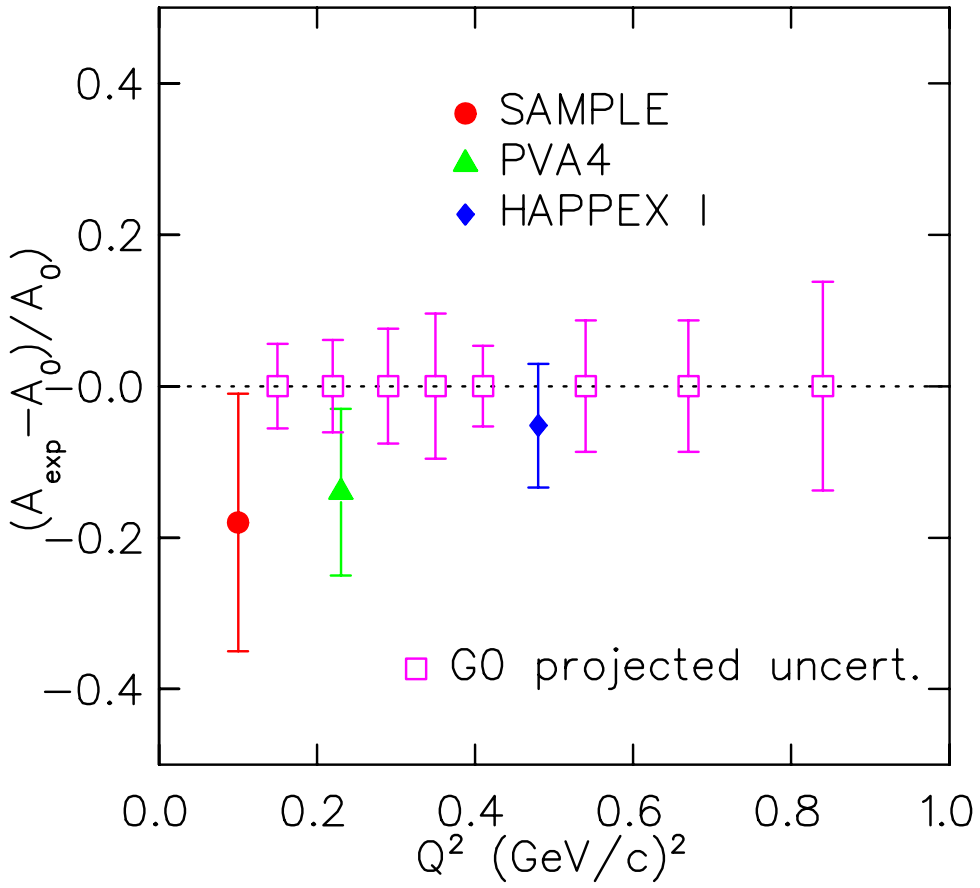

Figure 2.4: A summary of the deviation of measured asymmetries from the expected (no strange quark) values For the measurements at higher momentum transfer, the calculation of Zhu, *et al.*[41] is used for the normalization of G_A^e; the momentum transfer dependence is taken to be the same as that measured in neutrino scattering.

3 Experiment

3.1 Introduction and Kinematics

In this experiment we propose to make measurements of the backward angle parity-violating asymmetries using both hydrogen and deuterium targets. The kinematics are chosen to approximately match the range of the forward angle running except for the very lowest momentum transfers (and beam energies) where the SAMPLE experiment has already made measurements [50, 10]. As shown in these measurements and discussed above (Section 2), measurements involving quasi-elastic scattering from deuterium are necessary to separate the vector and axial vector currents of the nucleon. The G0 experimental program therefore includes, in addition to the recently completed forward angle measurement, backward angle measurements with both targets.

We propose to make these backward angle measurements at three values of Q^2 (elastic in the case of the hydrogen target, quasi-elastic in the case of deuterium) to give a reasonable amount of information on the Q^2 variation of the three form factors G_E^s, G_M^s and $G_A^e(T = 1)$. The nominal central angle for the G0 spectrometer for these measurements is 110°, thus fixing the incident energies. The kinematics, (quasi-) elastic rates (for the entire spectrometer acceptance), and nominal asymmetries for these three running conditions are shown in Table 3.1

Target	E (GeV)	θ (°)	Q^2 (GeV^2)	Rate (MHz)	Asymmetry (ppm)
^{1}H	0.424	110	0.3	2.03	−18
^{2}H	0.424	110	0.3	2.80	−25
^{1}H	0.585	110	0.5	0.718	−32
^{2}H	0.585	110	0.5	1.100	−43
^{1}H	0.799	110	0.8	0.190	−54
^{2}H	0.799	110	0.8	0.274	−72

Table 3.1: Elastic and quasi-elastic kinematics, rates, and nominal asymmetries.

The new experimental aspects of this measurement (as compared to the forward angle measurements where the asymmetries are significantly smaller) are associated with the quasi-elastic scattering from deuterium. Accordingly, in the remainder of this section, we address only the corrections necessary to extract single nucleon information from the quasi-elastic scattering as well as the requirements for particle identification accruing from the quasi-free π^- production from the neutrons in the target.

3.2 Deuterium corrections

Because the third asymmetry measurement that allows separation of the three weak form factors involves a nuclear target, there are potentially nuclear corrections to be considered. These corrections fall into two categories: contributions from processes other than quasielastic scattering, such as elastic, threshold breakup and Δ production, and those that arise in quasielastic scattering but from non-nucleonic currents in the deuteron, such as meson exchange.

The experimentally measured asymmetry can be written as

$$A_D = \frac{\sigma_{QE} A_{QE} + \sigma_{el} A_{el} + \sigma_{ted} A_{ted} + \sigma_\Delta A_\Delta}{\sigma_{QE} + \sigma_{el} + \sigma_{ted} + \sigma_\Delta} \tag{3.1}$$

where the four terms are contributions from quasielastic scattering, elastic e-d scattering, threshold breakup, and Δ production, respectively. Nucleon resonances higher than the Δ are not considered.

The asymmetry due to elastic e-d scattering was calculated by Pollock [65] and in [5], and, neglecting the small D-state contribution to the deuteron wave function, can be summarized by the expression

$$A_{el} = \frac{G_F Q^2}{4\pi\alpha\sqrt{2}} \left[4\sin^2\theta_W + \frac{2G_M^s}{(G_M^p + G_M^n)} F_T \right] , \tag{3.2}$$

where $F_T = v_T B(Q^2)/(A(Q^2) + B(Q^2)\tan^2(\theta/2))$, where $A(Q^2)$ and $B(Q^2)$ are the elastic deuteron form factors, and v_T is the usual kinematic factor. The asymmetry for threshold breakup was also calculated in [5] and may be written as

$$A_{ted} = -\frac{G_F Q^2}{4\pi\alpha\sqrt{2}} \left[(2 - 4\sin^2\theta_W) - \frac{v_{T'}}{v_T}(4 - \sin^2\theta_W)\frac{M_N}{q}\frac{G_A^e(T=1)}{2G_M^{T=1}} \right] \tag{3.3}$$

where $v_{T\prime}$ is the standard kinematic factor. Although in each case there is some dependence on the unknown form factors G_M^s and G_A^e, both asymmetries are comparable in magnitude to A_{QE}. The effect of such events on A_D is negligible: in the worst case the elastic (threshold) cross sections are 3% (0.1%) of the integrated quasielastic cross sections.

The inelastic scattering contribution, which will arise primarily from Δ excitation, can potentially modify the measured asymmetry from that expected from quasielastic scattering alone and can likely not be neglected. The asymmetry in hydrogen is the subject of the proposal of S. Wells *et al.*, [66], where the formalism for parity violation in the N-Δ transition is documented. Following the notation of Mukhopadhyay, *et al.* [67],

$$A_\Delta = -\frac{G_F Q^2}{4\pi\alpha\sqrt{2}} \left[\Delta_{(1)}^\pi + \Delta_{(2)}^\pi + \Delta_{(3)}^\pi \right] \tag{3.4}$$

The two terms $\Delta_{(2)}^\pi$ and $\Delta_{(3)}^\pi$ combined are expected to be $\sim 0.2\Delta_{(1)}^\pi$, and are thus neglected for the purposes of the background calculation. The quantity $\Delta_{(1)}^\pi = 2(1 - 2\sin^2\theta_W) = 1.075$ [11]. In [68], A_Δ in a nucleus was considered. At backward angles, the dominant contribution is from quasifree Δ production, so $A_p \sim A_n \sim A_d$.

The contribution to the asymmetry from quasifree Δ production was estimated by simulating the detector acceptance for both elastically and inelastically scattered electrons in the CED and FPD arrays. These events result in two bands in FPD/CED space with very little overlap at the two lowest kinematics, somewhat more overlap at $Q^2 = 0.8$ (GeV/c)^2. The FPD/CED pairs corresponding to elastic scattering were then selected and each rate summed over all such pairs. The contribution from inelastic scattering is small except at the highest momentum transfer, where such events are expected to result in a reduction of the measured asymmetry in the elastic region of FPD-CED space of about 10%. It is important to note that, just as in the case of the hydrogen data, the inelastic asymmetry in deuterium will be measured simultaneously with the quasielastic scattering asymmetry over a range of Q^2 and ν, so it will be possible to make any necessary correction with measured inelastic asymmetries rather than relying on a calculation.

The second major class of corrections to be considered are corrections to the simple "static approximation" for the deuterium asymmetry:

$$A_d = \frac{\sigma_p A_p + \sigma_n A_n}{\sigma_d} \tag{3.5}$$

In this expression the deuteron is assumed to consist of a noninteracting neutron and proton at rest. Hadjimichael, *et al.* [7] have considered the effect of final state interactions on this expression. They performed their calculation with two nucleon potentials that represent the extremes of the state-of-the-art potentials. Near our kinematics, they find that the correction to the static asymmetry expression is small ($\sim 1\%$), and the variation between the two nucleon potentials used is also small ($\sim 1\%$). Two body currents (meson exchange currents) have been considered by the authors of refs [61, 8]. Schramm and Horowitz [61] considered heavy meson exchange corrections; they find that the correction to the asymmetry is less that 1% at our momentum transfer. The most recent work [8, 9] which also incorporates pion exchange currents also finds that the corrections are small.

Finally, there is the possibility of an asymmetry generated by a nuclear parity-violating component in the deuteron wavefunction. This effect has been calculated in refs [62, 63] and shown to be small compared to our expected asymmetries. For example, Hwang, *et al.* [63] used the DDH [64] parameters to characterize the parity-violating nucleon-nucleon interaction, and they find that the asymmetry is $A \sim 4 \times 10^{-7}$ at backward angles at 0.500 GeV for relative energy $E_{np} = 9$ MeV. The asymmetry falls with increasing E_{np}, so it will be even less significant at the quasielastic peak.

3.3 Particle identification requirements

Negatively charged pions have been found to produce a significant background to the elastic and quasielastic rates detected by the G^0 spectrometer at backward angles. The pions are produced mainly by photoproduction near the Δ-resonance. In the case of a hydrogen target, single π^- photoproduction is forbidden by kinematics; two pions must be produced in order to see a single π^- in the spectrometer. However, in the case of a deuterium target, single π^- photoproduction occurs due to the presence of neutrons.

This background is found to dominate over quasi-elastic rates from deuterium at backward angles. The background can be kinematically separated from elastics in the hydrogen target case, but tends to overlap with the inelastic electrons in the measurement of the parity violating asymmetry in the $N \rightarrow \Delta$ transition [66]. It is therefore desirable to have an additional particle identification detector for the backward angle experiment.

3.3.1 Calculation of π^- Cross Sections

The process of π^- photoproduction from the neutron can be simulated using photoproduction cross-sections with the appropriate Bremsstrahlung and virtual photon fluxes. These processes were used both for the deuterium itself and for (quasi-free) production from the aluminum target windows in each case.

For the virtual photon contribution to the cross section, the MAID [69] parameterization of the transverse photoproduction pion cross section was used with a virtual photon flux [70] and appropriate Jacobian factors. Fermi motion was included in the model, using Monte Carlo generation of initial state nucleon momenta, according to a nucleon momentum distribution obtained from a fit of inclusive quasi-elastic scattering data.

For the Bremsstrahlung photon contribution to the cross section, the GRAAL Monte Carlo generator was used [71]. This generator was found to be in good agreement with a model using the photoproduction cross section from MAID and the Bremsstrahlung photon spectrum of Ref. [72]. The GRAAL Monte Carlo code has the additional capability of simulating two-pion production.

These cross sections were also tested against the commonly used code of Lightbody and O'Connell (LBOC) [73]. For kinematics similar to those encountered in G^0, the MAID and GRAAL results were found to be a factor of 3 to 4 larger than those given by the LBOC code. This was determined to be due to the older pion photoproduction cross-section parameterization used in the LBOC code, and due to bugs in the LBOC code.

3.3.2 Measurement of π^- Rate at Backward Angles

To test the pion photoproduction cross-section calculation in kinematics similar to those planned for G^0 backward-angle running, a facility development request to use the Short-Orbit Spectrometer (SOS) in Hall C was generated. During a parasitic run on October 27-29, 2000, π^- photoproduction cross sections from hydrogen, deuterium, and carbon targets were measured. Elastic and quasielastic cross-sections were also measured. For these measurements, the beam energy was 0.824 GeV, and the SOS angle was fixed at 136.5°. Rates for negatively charged particles were measured in the momentum range 150 to 400 MeV/c. The beam current averaged 20 μA. Data for hydrogen and deuterium were taken with two different target lengths (4 and 15 cm) to test the ability of the calculations to accurately predict the fractions of the total pion rate due to virtual photons and Bremsstrahlung photons.

The results and analysis of the pion data from this run are reported in a G^0 internal note [74] and will be summarized here. The measured π^- cross sections from hydrogen are

shown in Fig. 3.1. The cross section is compared with a calculation using the GRAAL

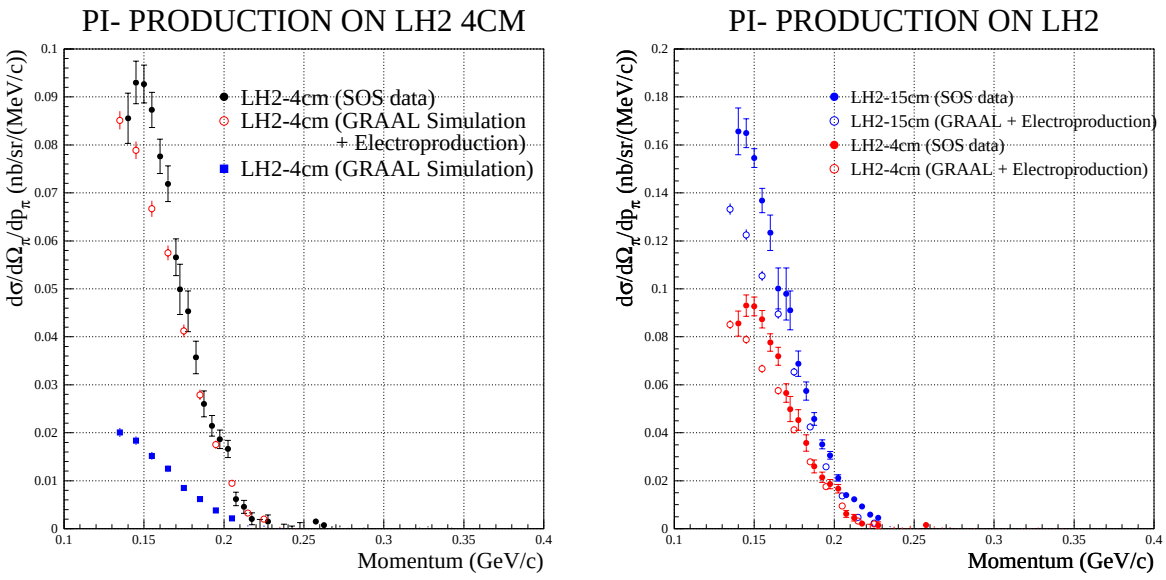

(a) (b)

Figure 3.1: Comparison of data and simulation of π^- production from (a) 4 cm and (b) 15 cm LH_2 targets.

code. The breakdown of electroproduction and photoproduction pieces of the cross section in the simulation is also shown. The disagreement at lower momentum is believed to be due to the fact that the GRAAL code does not presently simulate virtual photons below a certain Q^2. The G^0 spectrometer will generally select pions of higher momentum, so the agreement is sufficient to be able to use the code to generate two pion production for simulation of backgrounds in the experiment.

The measured π^- cross sections from deuterium are shown in Fig. 3.2. The cross sections are compared with the simulation using the GRAAL code for pion photoproduction and the MAID-based calculation for pion electroproduction. The cross section is dominated by single π^- production. The agreement of the data with the calculation is excellent, indicating that the cross section for the G^0 case is well understood.

The ratio of the pion rates from the 15 cm and 4 cm liquid hydrogen and liquid deuterium was found to be roughly 1.6, in agreement with arguments based on the radiation length of the target and the equivalent radiator for virtual photons at these kinematics.

3.3.3 Pion Rates and Contaminations

Pion rates for G^0 backward angle running were determined using the models of the cross section tested in the previous section, along with a GEANT-based model of the G^0 acceptance [75].

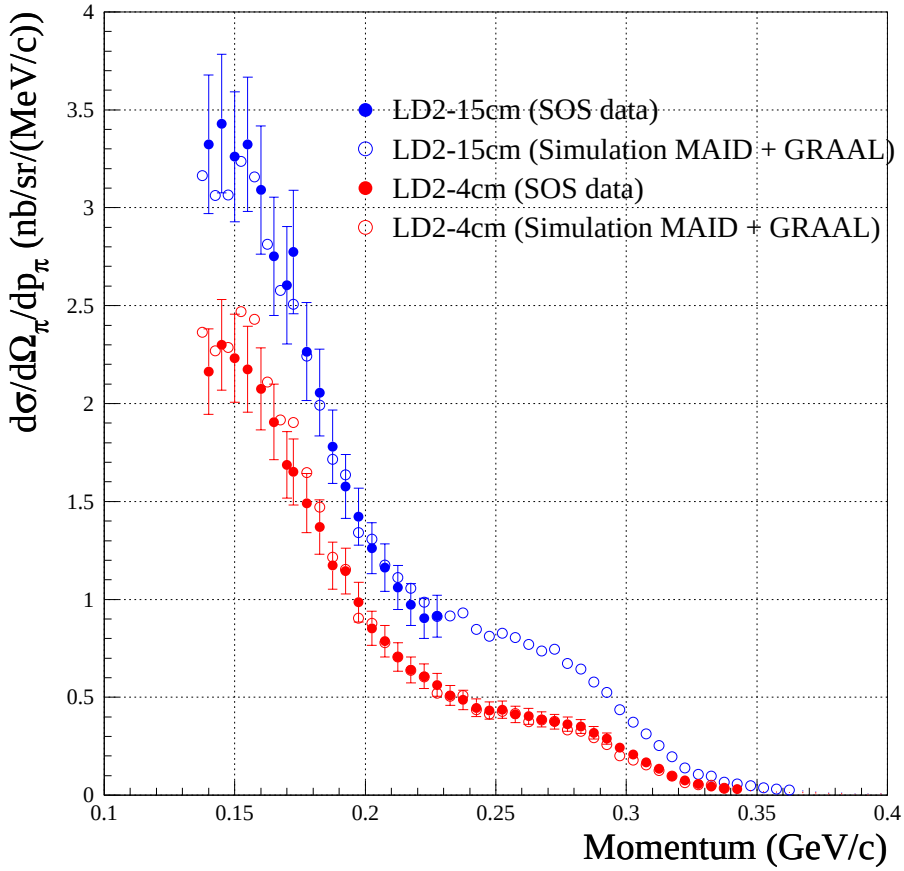

Figure 3.2: Comparison of data and simulation of π^- production from 4 cm and 15 cm LD_2 targets.

The pion rates for the liquid hydrogen target running are found to be largest relative to the elastic rate for the proposed beam energy of 0.799 GeV. The pion, elastic electron, and inelastic electron rates for 0.799 GeV are shown in Fig. 3.3. Rates are proportional to the size of the box shown for each CED and FPD combination. The rates assume a 20 cm long target and 40 μA beam current. Tracking of all secondaries was included. Muons resulting from pion decay are also included in the pion rates. At 0.799 GeV, muons present 15% of the total flux of pions and muons at the location of the CED. At 0.424 GeV, 20% of the total flux is due to muons. The pion rates are found to be roughly 25% of the elastic rate along the locus of the elastic curve at 0.799 GeV.

The pion rates for LH_2 running are dominated by contributions from the aluminum target windows. For this simulation, only the contribution of virtual photons interacting with the target windows was included, and final state effects and Fermi motion were ignored. Inclusion of real photons increases the pion rate by a factor of 1.5, but final state interactions should reduce the cross section by roughly 50%, so these two effects roughly cancel.

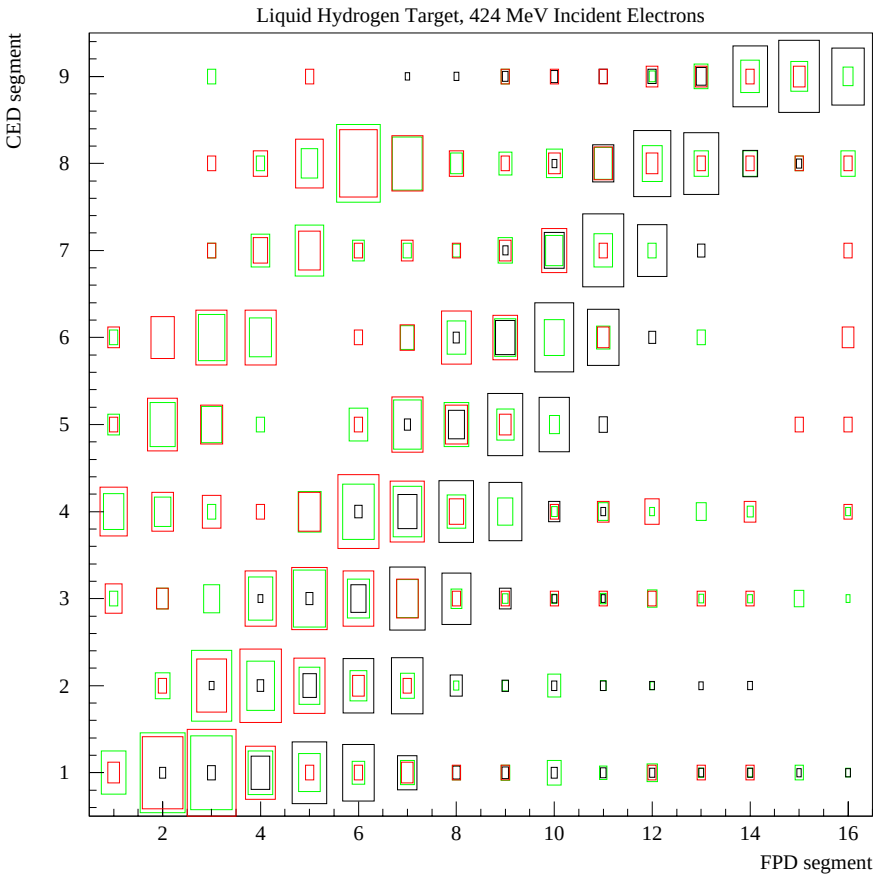

Figure 3.3: Relative CED and FPD rates for one octant of the G^0 spectrometer, LH_2 target, for beam energy 0.799 GeV. The coincidence rate is proportional to the size of the box. Elastic e^- rates are shown in black, inelastic e^- rates are shown in red and estimated π^- rates are shown in green.

The effect of Fermi smearing does not change the overall rate, but causes the pions to have more overlap kinematically with the elastic electrons. The effect of this will be discussed later.

The π^- rates for LD_2 running are shown in Figs. 3.4(a), (b), and (c) for the proposed beam energies of 0.424, 0.585, and 0.799 GeV, respectively. As expected, the negative pion rates are considerably larger for liquid deuterium. The aluminum target windows account for roughly 1% of the total rate, with the remaining 99% being roughly equally divided between contributions from virtual photon and Bremsstrahlung photon fluxes to the π^- photoproduction cross section from the LD_2 in the target itself. There is a large pion contamination in all three cases, preventing the measurement of the quasi-elastic asymmetry for the deuteron in the absence of additional particle identification (the aerogel Cherenkov detector is discussed in Section 4.1.3).

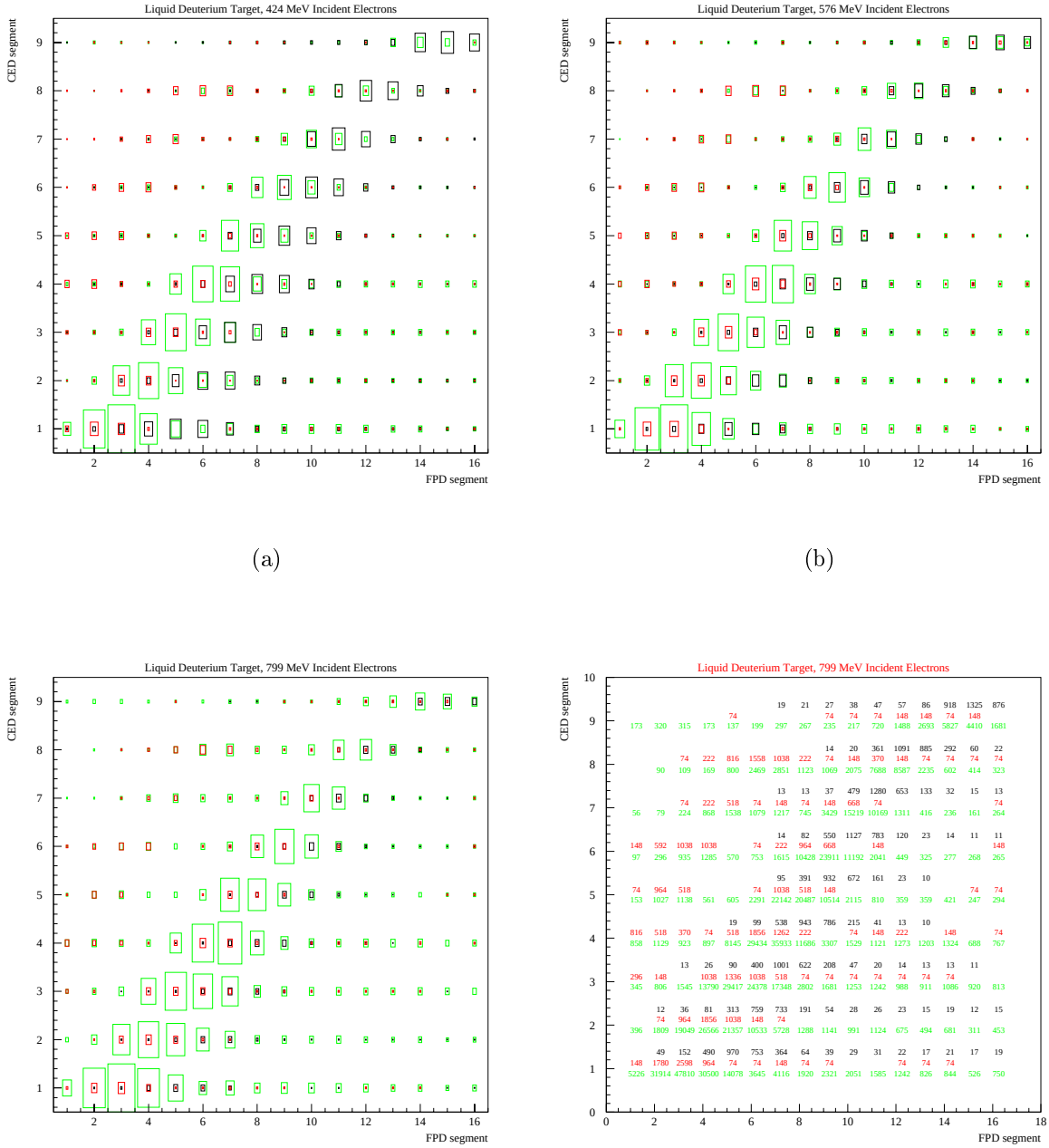

Figure 3.4: Relative CED and FPD coincidence rates for one octant of the G^0 spectrometer, LD_2 target. The coincidence rate is proportional to the size of the box. Quasi-elastic e^- rates are shown in black, inelastic e^- rates are shown in red and estimated π^- rates are shown in green. (a) 0.424 GeV, (b) 0.585 GeV, (c) 0.799 GeV. Figure (d) contains the rates for 0.799 GeV, in text form.

Selecting certain CED and FPD combinations allows the optimization of the elastic/inelastic separation. The same selection procedure also helps to exclude pions from the elastic sample. Table 3.2 summarizes the pion contaminations expected for the proposed kinematics, satisfying the same cuts used to separate elastic from inelastic electrons described in Section 2. As mentioned earlier, the pion contamination for the liquid hydrogen

$E_{\rm beam}$	$(\pi+\mu)/e$ ratio	
(GeV)	LH_2	LD_2
0.424	0.013	0.39
0.585	0.042	1.6
0.799	0.25	8.4

Table 3.2: $(\pi+\mu)/e$ ratio expected for same CED and FPD combinations used in Section 2 to attempt to separate elastic from inelastic electrons. Here only elastic and quasi-elastic electrons are counted in the denominator.

target running is dominated by contributions from the target windows. The contribution from two-pion production in the liquid hydrogen target itself to the total pion rate is 15% at 0.799 GeV, but is negligible at lower energy. As mentioned earlier, the effect of Fermi-smearing of the kinematics of these pions was neglected. Fermi smearing of the pion kinematics has been estimated to give roughly a factor of 2 increase in the contamination, for the lowest beam energy proposed. The relative size of the effect will be smaller at higher energy, as the Fermi momentum becomes small relative to the beam energy. The estimated pion contaminations for LH_2 should therefore be accurate to the 50% level.

The pion contamination for LD_2 *was* calculated including Fermi motion. As already noted, this contamination is found to be too large to make a measurement of the quasi-elastic asymmetry in deuterium as the pion to elastic electron ratio is 8.4:1 in the worst case. A particle identification detector must provide a pion rejection of better than 100:1, to reduce the worst-case pion contamination to the level of 10%.

The pion contamination of the inelastic electron rate from LH_2 is obviously worse than for the elastic case. The proposed measurement of the parity violating asymmetry in the $N \to \Delta$ transition [66], using the LH_2 running, would therefore also benefit from additional particle identification [76].

3.3.4 Rejection of π^- Background

The kinematics of the pions and muons which need to be rejected for each proposed beam energy are shown in Table 3.3. The type of detector affording the best π/e discrimination at these energies and the simplest implementation in the current G^0 geometry is an aerogel Cherenkov counter. The index of the aerogel should be less than $1/\beta$ (see Table 3.3), but should be as large as possible to maximize light yield. It is therefore found that $n = 1.03$ is a good choice. An aerogel Cherenkov counter should also be able to give the requisite better than 100:1 pion rejection. The design and prototyping of the Cherenkov counters for G^0 will be discussed in Section 4.1.3.

E_{beam} (GeV)	p_π range (MeV/c)	$\beta_\pi^{\max}$	p_μ range (MeV/c)	$\beta_\mu^{\max}$
0.424	100 - 250	0.87	50 - 225	0.90
0.585	100 - 300	0.91	50 - 275	0.93
0.799	100 - 375	0.94	50 - 350	0.96

Table 3.3: Pion and muon kinematics for each spectrometer setting. Recall that muons account for less than 20% of the total pion and muon flux.

4 Apparatus

4.1 Detectors

The detector system to be used for these backward angle measurements consists of two arrays of scintillators and an aerogel Cherenkov detector for each of the eight G0 octants. The two scintillator arrays comprise: a Focal Plane Detector (FPD) array (sixteen detectors per octant each viewed from two ends), which have been used for the forward angle measurements, and a Cryostat Exit Detector (CED) array (nine detectors per octant each viewed from two ends). For backward angle electron detection, both arrays are required to determine the electron scattering angle and momentum, thereby providing an adequate separation between elastically and inelastically scattered electrons. The Cherenkov detector is required to reduce the contribution of π^-'s, particularly important during running with the deuterium target.

4.1.1 FPDs

In the forward angle measurement, back-to-back pairs of FPD scintillators are used to detect protons. In the back angle measurement 16 single FPD scintillators will be paired with CED scintillators to detect elastic and inelastic electrons as indicated below (the back element of each FPD pair will not be used in the back angle measurement). A photograph of completed North American (NA) and French FPD octants is shown in Figure 4.1; the octants are supported from a detector support ("ferris wheel") shown in Figure 4.2. Each FPD scintillator has a curved shape roughly 60 - 120 cm in length and a width of 5 - 10 cm. The first four FPD elements are 5 mm thick; the remainder have a thickness of 1 cm. Each is connected to a pair of photomultiplier tubes via lucite lightguides. The measured yield at each phototube is of order > 75 p.e. for minimum ionizing particles. These detectors performed as expected in the forward angle G0 run.

4.1.2 CEDs

The CEDs are a critical component of the G0 backward angle running, and here we provide a summary of the progress to date on this detector package. There are nine CEDs that, together with the FPDs, define the momentum and scattering angle of the detected electrons thus allowing for separation of elastic and inelastic events. With front end electronics composed of gate arrays (see Section 4.2), we are able to record events for given pairs of CED/FPD combinations, and thereby measure asymmetries for both elastic and inelastic events.

The design and construction of the CED elements has been completed. A detailed simulation of expected light yield from these detectors was first performed, and the number of photoelectrons predicted was found to be more than adequate for these measurements [77, 78].

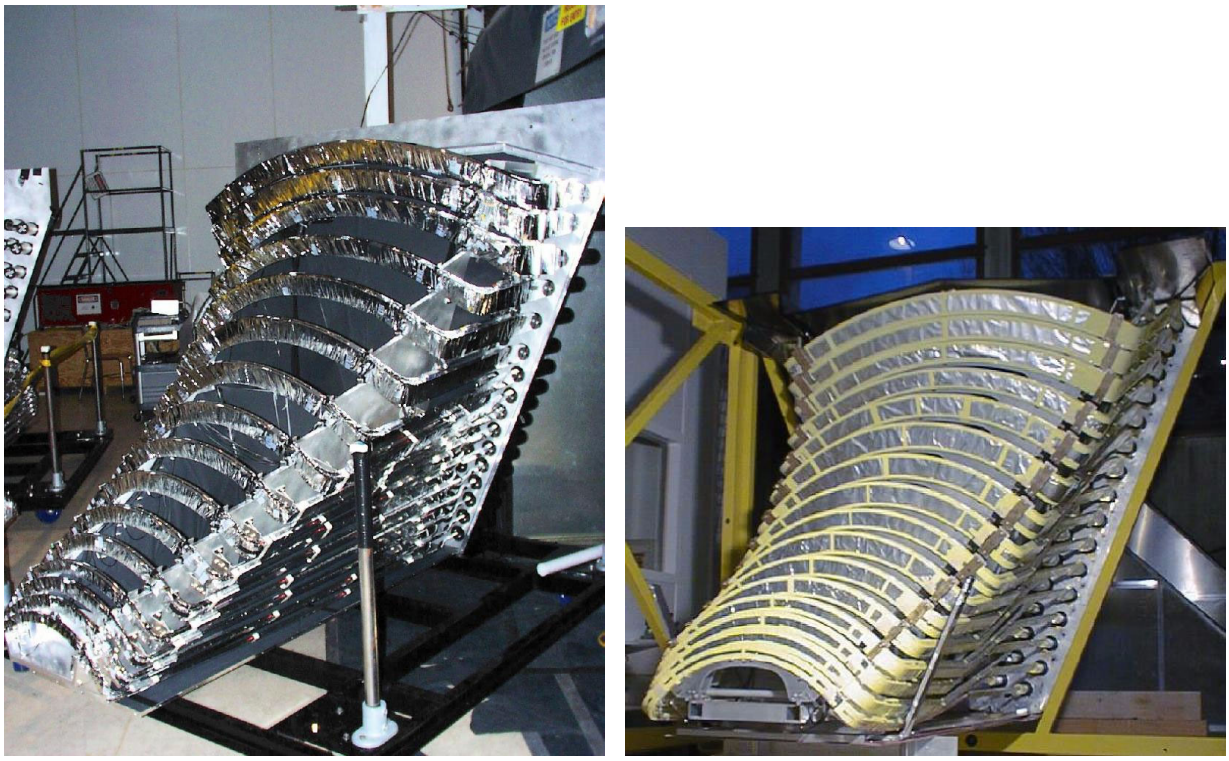

(a) (b)

Figure 4.1: Photograph of complete sets of FPDs mounted into the FPD octant support; a) North American b) French.

A prototype CED was constructed at TRIUMF, and tested at Louisiana Tech University using the same PMT/base assemblies to be used in the North American FPDs, and the amount of light collected was consistent with the predicted amount.

The procedure for manufacturing the correct shapes for the detectors and light guides was also developed and tested in the construction of the prototype CED. All scintillators and light guides, manufactured at TRIUMF, are now at JLab and assembly of the first octant has begun.

The design of the octant support structure for the CEDs is also complete. The design, a schematic of which is shown in Fig. 3, takes into account both the required mechanical support of the CED scintillator/light guide/PMT and base assemblies, as well as the relatively weak alignment constraints on these detectors. Also shown in this figure are the relative positions and shapes of the CEDs, light guides, and PMT's. Each octant support will be attached to the outer ring of the ferris wheel to provide the main mechanical support in the region of the CED assembly near the PMT's where the majority of the weight of these detectors resides. The positioning of the scintillators, as well as additional mechanical support, is obtained through the use of cantilevered struts extending from the main support through the region near the bend in the light guides and outside of the acceptance of the

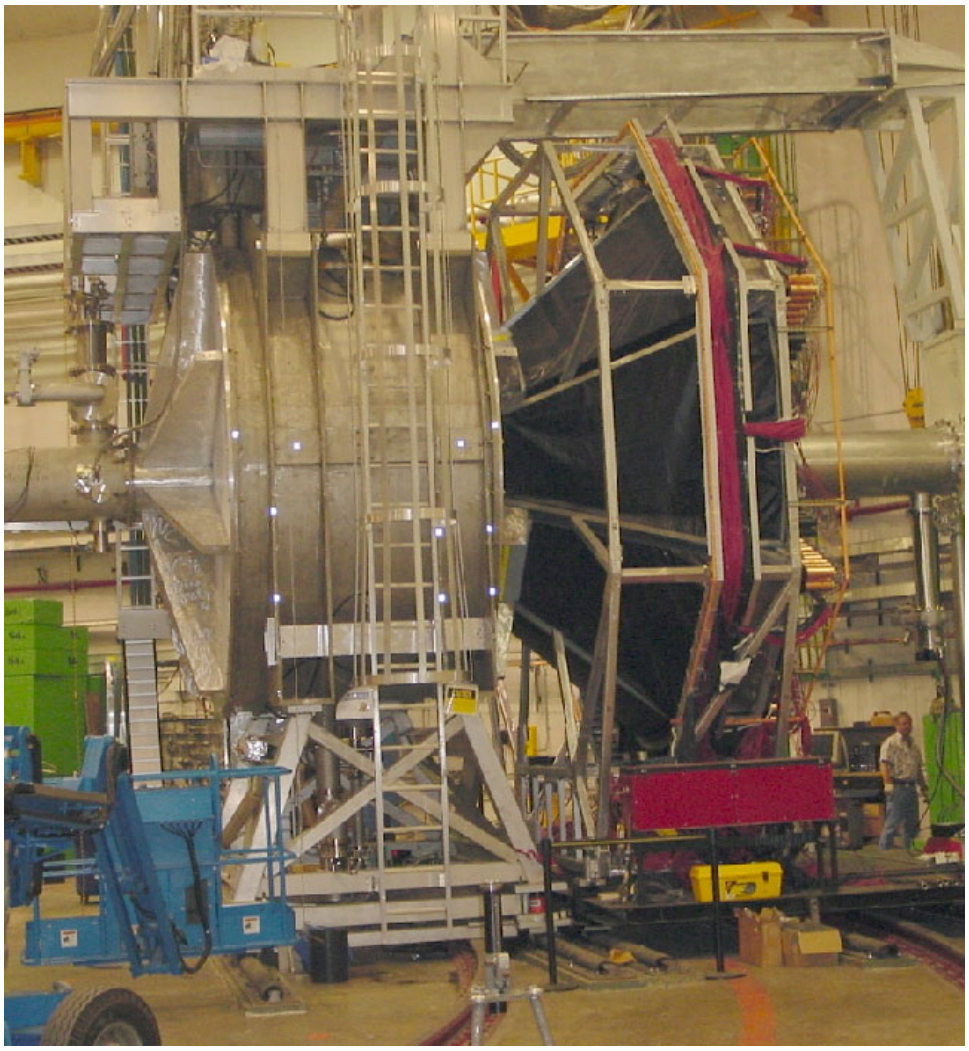

Figure 4.2: Photograph of G0 magnet and detectors in forward configuration.

scattered electrons. This octant support design is integrated with the support structure for the Cherenkov detectors. As part of the design process, the entire support structure was also prototyped in conjunction with developments discussed above.

4.1.3 Aerogel Cherenkov

The π^- background from $(n(e,\pi^-)e'p)$ will be reduced by introducing cuts in CED-FPD space, but not to a level sufficient to isolate quasi-elastic electrons. Therefore an aerogel Cherenkov detector has been designed to provide pion rejection across the full G0 momentum range, up to $\sim$ 400 MeV/c for $Q^2 = 0.8$ GeV^2. This, of necessity, must be an eight-sectored array of individual Cherenkov detectors mounted in conjunction with the CED-FPD sectors. The Cherenkov is located between the CEDs and FPDs and its mounting is part of the overall extension of the ferris wheel discussed above. The geometry of

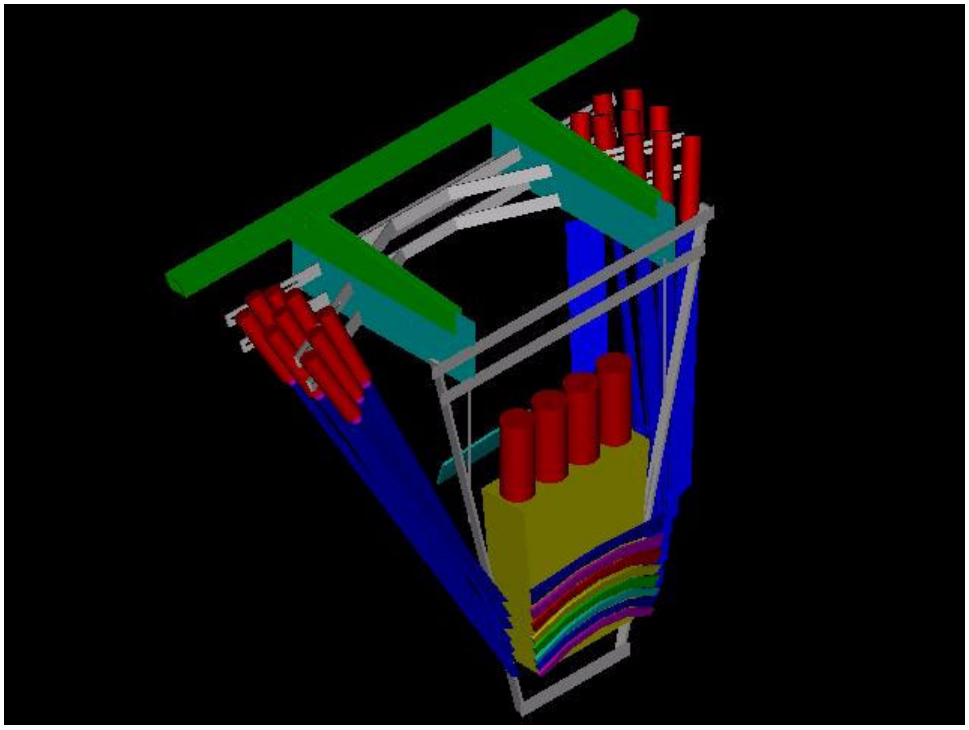

Figure 4.3: Schematic diagram of the CED octant support structure, showing the relative locations of the scintillators, light guides, and PMT's. Also shown is the relative position of a Cherenkov detector for backward-angle measurements.

the overall system is shown in Figure 4.4. A single Cherenkov detector is shown in more detail in Figure 4.5.

Negatively charged particles entering an octant of the G0 spectrometer pass through 5 cm of aerogel. The aerogel has a proposed index of refraction $n = 1.03$, so that a particle with a speed such that $\beta > \frac{1}{1.03}$ will produce Cherenkov light. Thus, pions up to a momentum of 570 MeV/c will not produce any light. On the other hand, all primary electrons will produce light. Thus the detector will operate in *coincidence* mode and not in *veto* mode.

The light is emitted within a small angle ($cos\theta_c = \frac{1}{1.03}$ at max.) and enters a downstream region whose walls are lined with a white diffuse reflector. The likelihood of a photon reaching one of four phototubes is related to their active area compared to the total internal area of the light box, which is a little better than 4%. Other goals in the box's design are to cover as large a fraction as possible of the G0 acceptance while keeping the timing spread as narrow as possible.

With 5 cm of clear aerogel, the electrons generate a signal of about 6 photoelectrons; whereas a 400 MeV/c pion would have a rejection factor of $\frac{1}{125}$. This latter pion signal is mostly due to δ-rays produced in the CEDs or elsewhere.

The phototubes for the Cherenkov counter for each octant are tied together to produce one summed signal. This signal is discriminated and ANDed into the trigger. Using existing

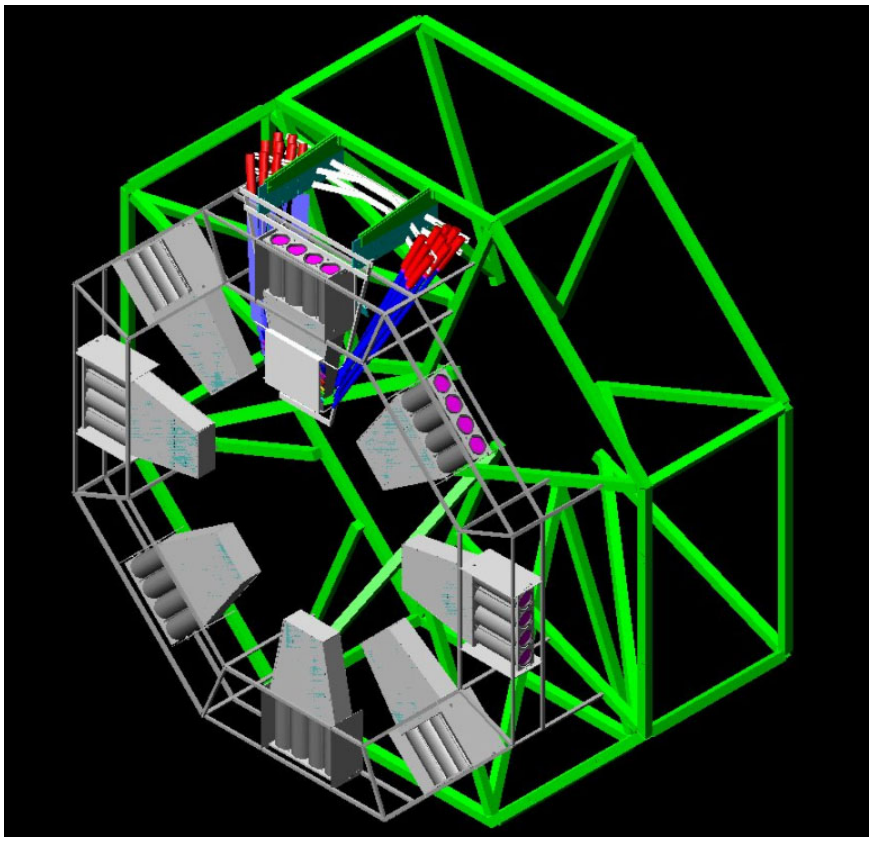

Figure 4.4: Concept of the full eight-sectored G0 backward angle set-up. The top sector shows the full detector arrangement: CED, Cherenkov and FPD. The others show the Cherenkov detectors only along with the 'ferris wheel' support frame.

sampling channels, Cherenkov ADC spectra will be used to check the calibration and pion rejection factor of each octant.

The typical time-width of the signal from these detectors is ∼20 ns (due mainly to collection time in the light box), during which time the radiator is 'dead'. This is because the light can bounce around in the box for some time. The rise time of the pulse is of the order of 1 ns.

Studies with both Monte Carlo simulation and prototypes of the Cherenkov counter have been done in France and at TRIUMF. Most of the assumptions above come from tests and simulations performed by the Caltech group and Grenoble simulations [79, 80]. At Caltech, a small Cherenkov test counter using a single phototube was built for the purpose of testing light yield and timing calculations from Monte Carlo simulations based on Ref. [81], and was found to produce results similar to the simulation. A first test detector was built at Caltech and tested at TRIUMF using a mixed particle test beam. An example of the results from this detector is shown in Figure 4.6 where the pion rejection is shown to be sufficient for our purposes. At TRIUMF a full size prototype was constructed and tested on the M11 $\beta \sim 1$ "electron" beamline. An example of the results from this test is presented in Figure 4.7, where the number of photo-electrons is shown for three different incident beam

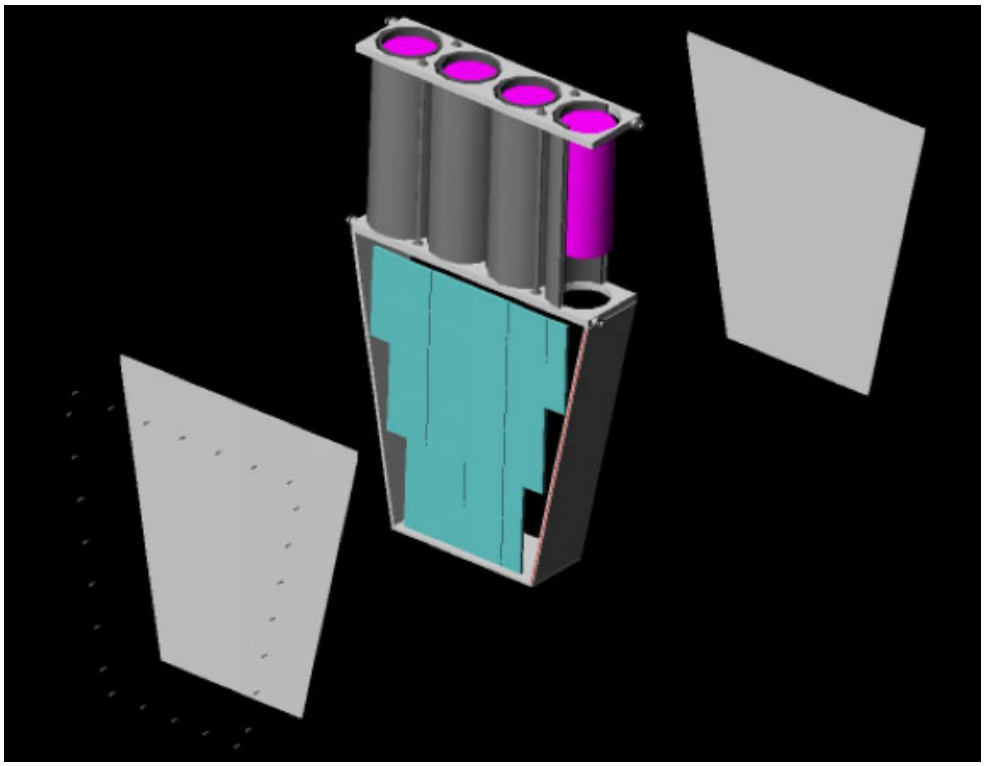

Figure 4.5: A view of the concept of a single octant light-box with aerogel Cherenkov radiator and PMT's

locations relative to the tubes. The French version of the detector is essentially identical, and similar test results have been obtained there.

All the parts for these detectors are either in-house (including Aerogel and phototubes) or are being manufactured. The French detectors will be shipped by the end of summer 2004, and the NA detectors will be assembled at JLab during the summer of 2004. A photograph of the first production French detector is shown in Figure 4.8.

4.2 Electronics

As in the case of the forward angle measurements the four French octants will be instrumented using electronics developed at IPN-Orsay (DMCH-16X boards, based on flash-TDC and DSP technology), while the North American octants will be instrumented with the relevant parts of the original Latching Time Digitizer (LTD) design. In particular, the DSP histogramming and scaler recording of events, respectively, of the two systems will be utilized. Additionally, all the PMT/base assemblies and associated power supplies used for the backing scintillator array for the FPDs will be used for the CEDs, and all of the instrumentation for the backing array (e.g., analog splitters, constant fraction discriminators, mean timers, and ADC and TDC channels for the monitoring electronics) is also available for the CED array.

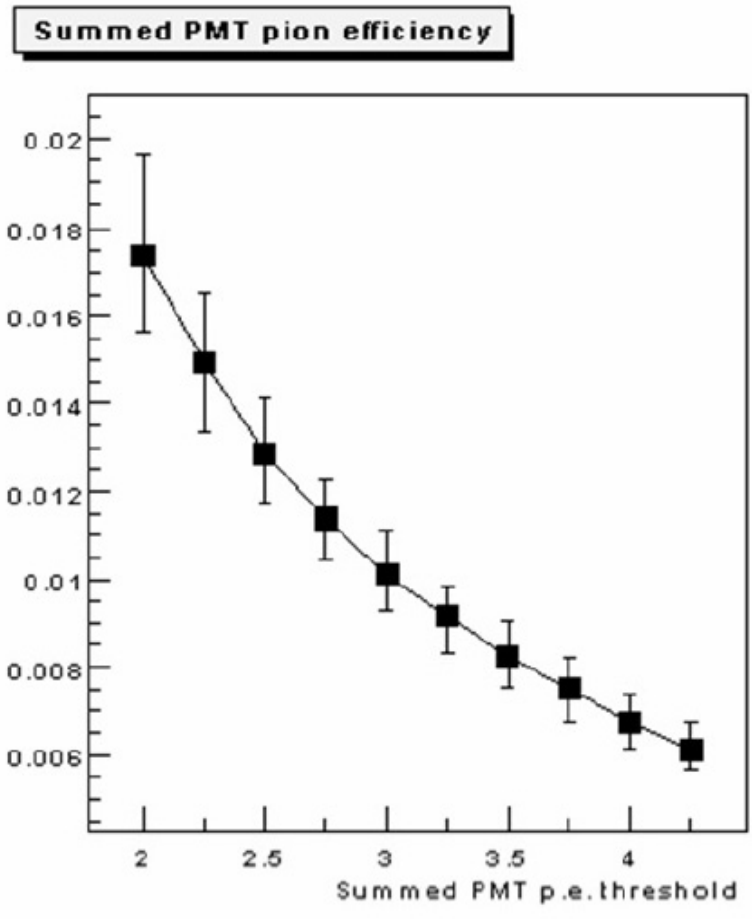

Figure 4.6: NA test Cherenkov results for pion rejection using the TRIUMF test beam.

The philosophy of the backward-angle electronics design is based in large part on the fact that the electrons being detected ($E_{scattered} \geq 200$ MeV) are all moving with approximately the same velocity, and therefore have a well defined flight time for each CED and each FPD. This is shown in Figures 4.2 and 4.10, where we plot the flight time from the target to selected CEDs and FPDs, respectively. There is a relatively tight time correlation can be made between a any CED/FPD pair. Consequently, the use of fast Programmable Logic Devices (PLDs) can provide hardware coincidences which can significantly reduce time uncorrelated backgrounds.

We have been able to use this relatively tight timing to make an important change to the front end of the electronics as compared with the original backward angle proposal. In order to take advantage of the more straightforward accelerator operation* and the possibility of higher beam currents, the standard 499 MHz pulse structure will be adopted for the backward angle measurements. Therefore, instead of using our beam pickoff signal as the

*The key operational difference for the accelerator is the reduced bunch charge allowing the prebuncher to be run at lower fields, etc.

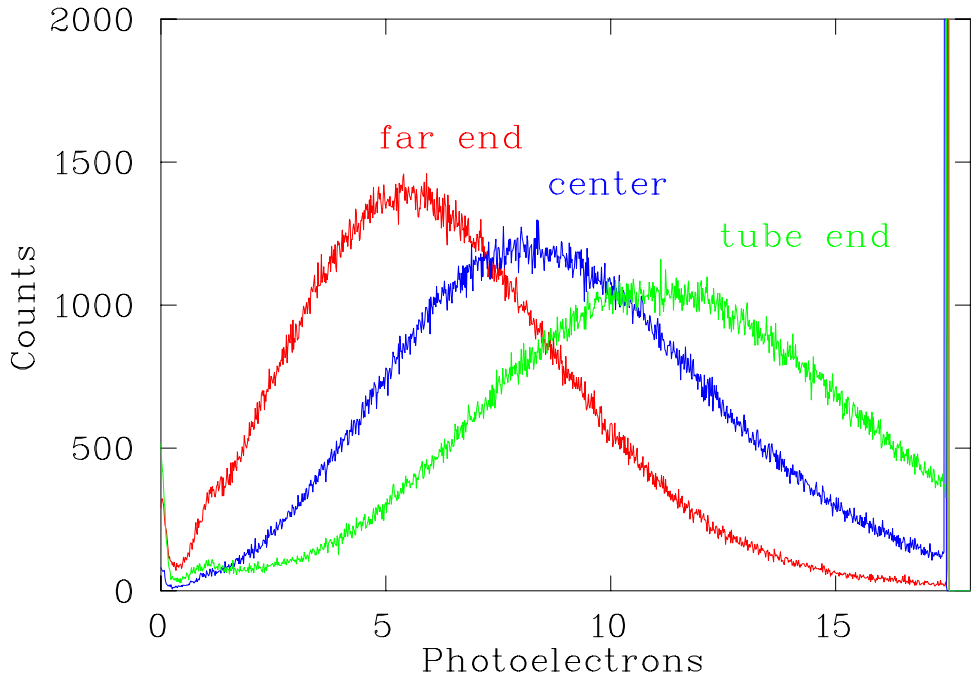

Figure 4.7: NA full-sized prototype Cherenkov results using the TRIUMF test beam.

primary electronics trigger, the mean-timer outputs of the CEDs for a given octant will be ORed together and ANDed with the ORed outputs of the FPDs for the same octant. The maximum total real rates per octant are shown in Table 4.1. Even with background rates in each CED and FPD of 500 kHz (maximum of background rates observed in forward angle run), the random coincidence rate per octant is only about 500 kHz (assuming 20 ns gates). Therefore with a total maximum trigger rate of order 1.7 MHz, the deadtime at the trigger level will only be 3%. Commercial electronics will be used to generate these trigger signals.

Target	E (GeV)	Rate (MHz)
^{2}H	0.424	1.18
^{2}H	0.585	0.58
^{2}H	0.799	0.39

Table 4.1: Approximate real rates *per octant* for LD_2 running including elastic electrons, inelastic electrons, pions and muons.

The North American electronics chain for forward-angle measurements is shown schematically in Figure 4.11. For the backward-angle measurements, the PMT's for the FPD backing detector array will be attached to the CEDs, and the LTD's and "munger" redistribution boards will be replaced by custom logic circuitry developed at Louisiana Tech. Thus, the input to this new logic circuitry is the output of the mean timers for both the FPDs and CEDs, a discriminated signal from the Cherenkov detector, and the main trigger signal as described above. The output of this new circuitry is sent to the latching scalers

Figure 4.8: Photograph of the first production French Cherenkov detector.

to count the number of coincidences between detectors in the CED array and those in the FPD array.

Significant development on the coincidence logic circuitry for the North American octants has taken place. The circuit has been designed and prototyped; production is now in progress. It involves the use of PLDs mentioned above, programmed to implement all the logic associated with the CED-FPD coincidences; the handling of "multiple hit" events (where more than one CED or more than one FPD fires for a given trigger); and dead time monitoring. The trigger pulse can provide a sufficiently small time window to enable the CED-FPD coincidences at the correct time of electron arrival at these detectors. The logic signal from the Cherenkov detector, which signifies that it was in fact an electron which fired both the CED and FPD involved in the coincidence, will be used to enable a latch which allows the coincidence information to be sent to the scaler modules. Additional counting of CED and FPD singles rates, with various combinations of multiple hit logic and Cherenkov signals included, will be used for an estimate of the front end electronics dead time.

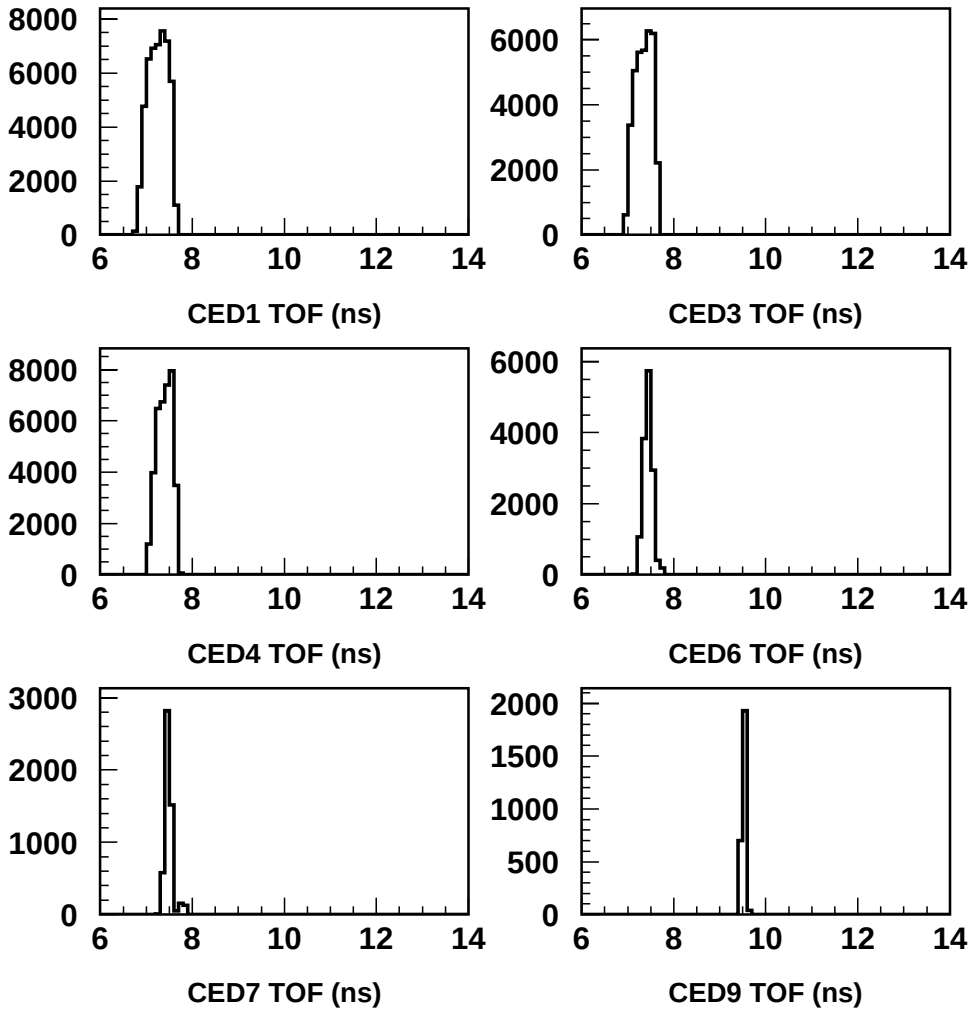

Figure 4.9: Flight times for electrons from the target to selected CEDs.

In the final configuration, a total of five boards will be needed per octant: one to handle the coincidence logic encoding; one to handle the multiple hit, Cherenkov, and dead time information; and three to handle TTL-ECL conversion to provide the appropriate level required by the latching scalers. All of the boards are housed in a custom VME chassis which provides the necessary power and common ground to each.

Nearly identical logic and overall philosophy will be used for the French electronics. For one octant, the front end instrumentation (discrimination and mean-timing) will be handled by two DMCH-16X boards. The meantimed outputs, available on the front panel, will be sent to a CED-FPD coincidence module (designed by the Grenoble group).

The coincidence board contains all PLDs and scalers needed for the counting of individual coincidences between each CED and each FPD. As in the North American design, the CED-FPD coincidences will be allowed during a short time window initiated by the trigger, and the Cherenkov counter will provide an enable signal for the counting. Also as in the North American design, additional counting associated with the singles rates in the CEDs and

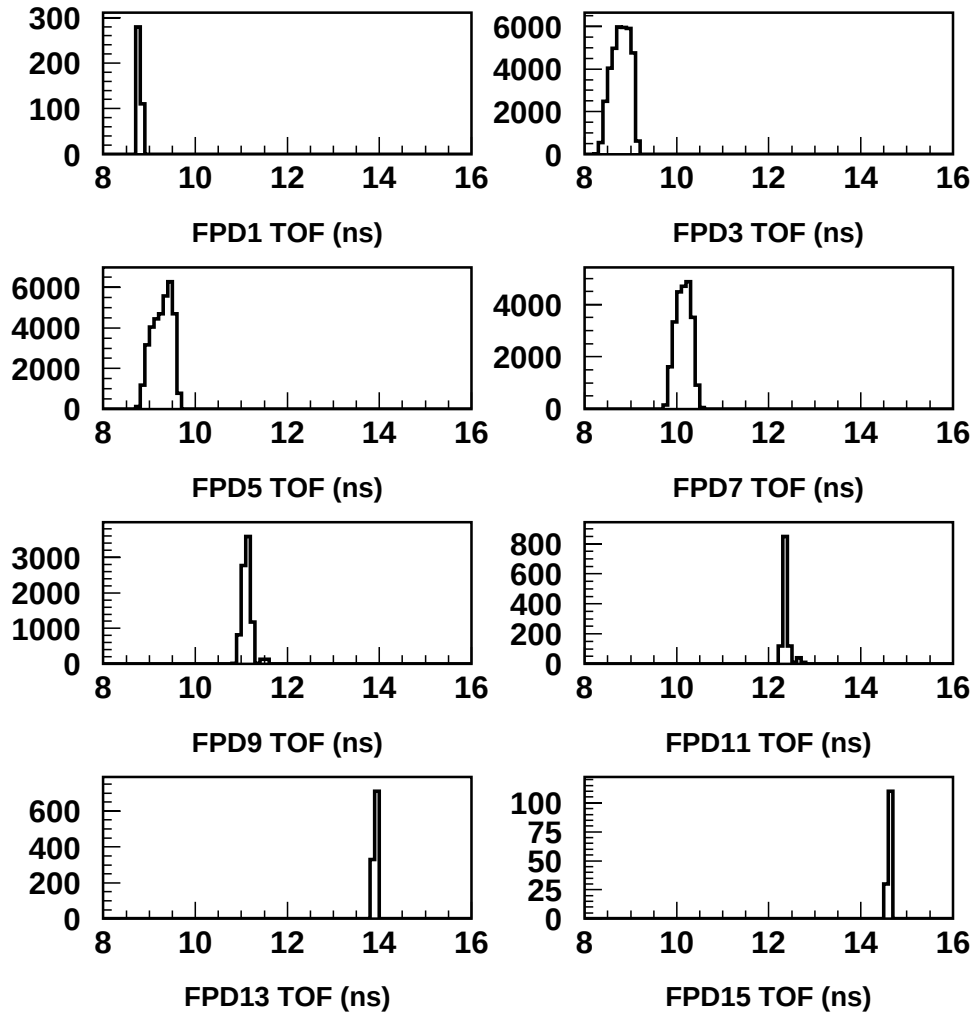

Figure 4.10: Flight times for electrons from the target to selected FPDs.

FPDs will be used for the estimate of the number of multiple hit events and for deadtime monitoring. In addition to the singles counting available in the coincidence board, the DMCH-16X modules also provide the time of flight information for the individual CEDs and FPDs, which can be used for an accurate estimate of the number of lost events due to the deadtime of the front end electronics.

One CED-FPD coincidence module will be able to handle two octants. For the four french octants, the VXI crate will therefore support eight DMCH-16X and two CED-FPD coincidence modules. Production of the CED-FPD coincidence boards is in progress – final testing of the first production board is being completed.

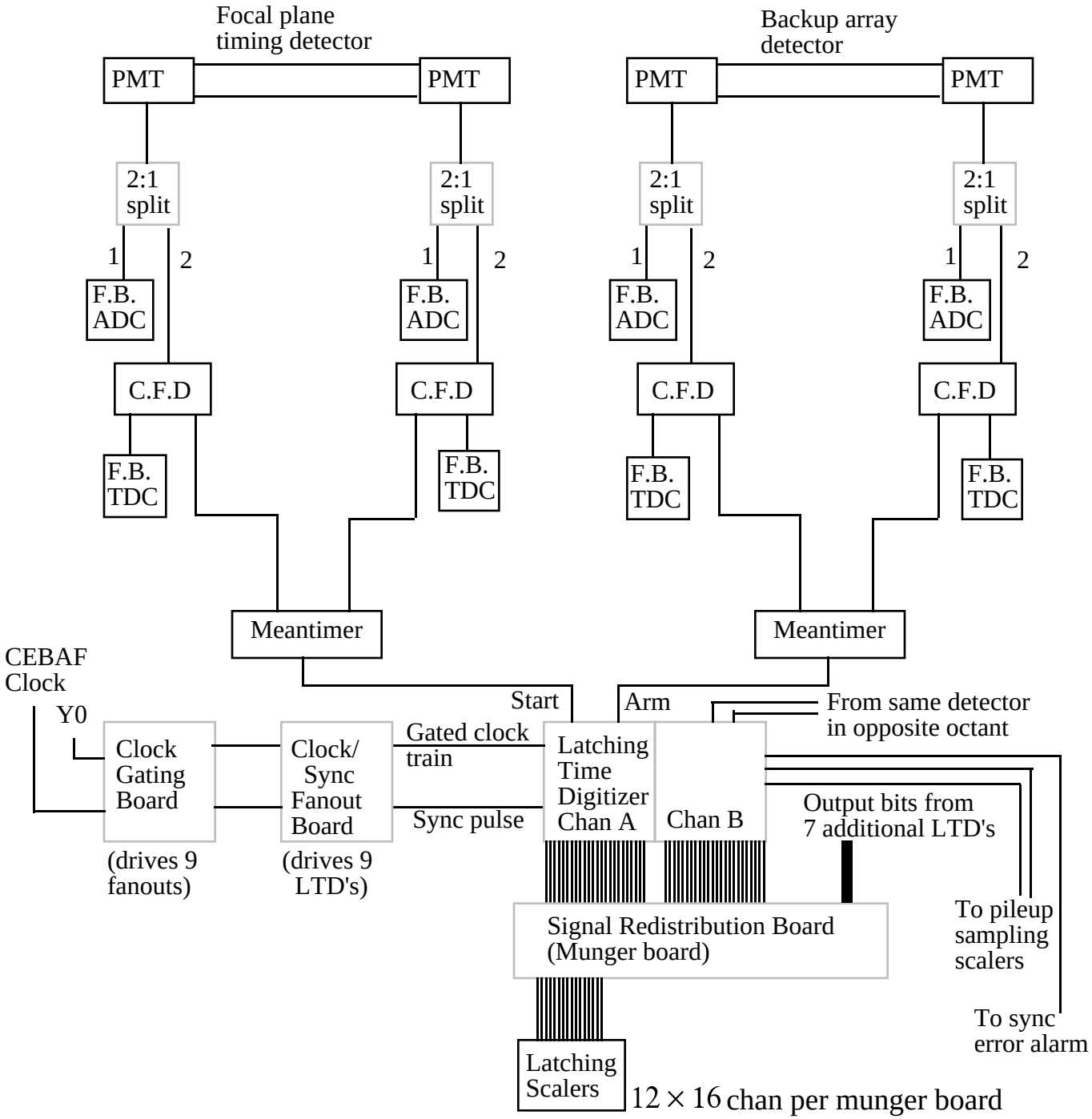

Figure 4.11: Electronics block diagram for the forward-angle running mode for the North American octants.

4.3 DAQ

The data acquisition requirements for the backward-angle running configuration are almost identical to those for forward-angle running. Only small differences in the data stream will be present for both the North American and French octants.

Generally, the data stream will consist of two different types of events: high statistics data counting all particles detected within each $\frac{1}{30}$ s macropulse period and read out at 30 Hz after being latched during a ~ 200 μs interval during which time the helicity Pockels cell may change polarity; and low statistics monitoring data including ADC and TDC spectra for each PMT on each detector read out at ~ 1 kHz.This is true for both forward and backward running configurations. There will in fact be less data arising from the monitoring electronics in the backward-angle running than in the forward-angle mode, simply because there are only 9 CEDs instrumented per octant (corresponding to 18 ADC and TDC spectra per octant) in contrast to 16 FPD backing detectors instrumented per octant in the forward-angle configuration. The small differences arising between the two running modes occur in the high statistics data only for the French octants, with no difference in the data streams for these events for the North American octants between the forward and backward running modes. To understand these differences, we review the data obtained for both types of instrumentation, and for both running configurations.

In the North American octants, the LTD boards discussed in the previous section are designed to separate the data obtained from each FPD for the forward-angle running into time bins within the 32 ns period between successive beam bursts. High speed scalers will then be used to store the time spectra. For the backward-angle running, no time encoding is necessary because all backward scattered electrons are moving with approximately the same speed, and it is impossible to separate elastically scattered electrons based on time of flight information. Thus, of the available scaler channels that were used for time bin counting during the forward-angle running, some will be used to count the number of coincidences between each CED and each FPD, and the remaining scaler channels will be used to count singles rates in each CED and FPD, with various constraints of multiple hits and Cherenkov detector firing. Different CED-FPD combinations correspond to different electron momentum, which allows an identification of the elastically and inelastically scattered electrons independently.

In the French octants, the high statistics data for the forward-angle measurements are sorted into time of flight histograms directly on the DMCH-16X boards through the use of flash TDC's and DSP's. These histograms are then sent into the data stream during the data read out every $\frac{1}{30}$ s through the VXI crate backplane. For the backward-angle measurement, the main information will come from scalers containing the CED-FPD coincidences and CED and FPD singles rates with multiple hit and Cherenkov constraints. The number of scalers needed is about the same as in the North American scheme.

Although there will be very little change in the data acquisition software for the backward angle running, there will be some change required to the analysis software. In the forward mode, the primary analysis involves construction of time-of-flight histograms from the North American scaler electronics or from the Orsay TDC data. Asymmetries are calcu-

lated for each detector from identification of the proton timing peak in the TOF spectrum. Since in the backward mode, in both the North American and French octants, the primary means of identifying events will now be scalers counting yields in each FPD/CED pair, asymmetries for each FPD/CED pair will be calculated from the scaler values. The processed data will thus be a two dimensional array of asymmetry values in FPD/CED space. Elastic and inelastic regions in FPD/CED space will be identified from the scaler yields.

4.4 Target

The backward angle running of the G0 experiment will utilize a slightly modified configuration of the liquid hydrogen target that has been used successfully for the forward angle measurements. It is important to note that unlike the spectrometer which is rotated for the backward angle measurement, the target system remains on the upstream side just as it was in the forward measurement. The baseline requirements for the G0 target remain (1) target length of 20 cm, (2) dissipation of heat deposited by 40 μA of electron beam current and (3) operation without introducing uncorrected false asymmetries at a level $> 5\%$ of the overall uncertainty in the measurement ($\Delta A \approx 10^{-8}$ over the entire run for any individual source of false asymmetry). The modifications required for backward angle running are:

- extension of the target support to longitudinally center the target in the magnet in the backward angle orientation (this extension pipe already exists),
- the port for the target service lines needs to be redesigned to accommodate the space constraints associated with the detector support structure,
- connection of gas panel to D_2 supply tank during LD2 runs.

The liquid hydrogen target cell is connected to a cryogenic loop to recirculate and cool the liquid. The hydrogen will be cooled through heat exchange with compressed helium gas. The liquid hydrogen is thus maintained at 20 K and 25 psia (through connection with the ballast tank). When full, the target cryogenic loop plus target cell and manifold will contain 6.6 liters of liquid hydrogen.

Figure 4.12 is a scale diagram showing the cryotarget centered within the liquid nitrogen shield of the superconducting magnet. The main components of the cryoloop are a pump for circulating the target fluid, a heat exchanger, the target cell, and a manifold to direct the fluid flow down the center of the target cell and back near the cell walls. The arrows in the figure indicate the direction of fluid flow in the loop.

The helium cell positioned adjacent to and just upstream of the liquid hydrogen cell serves three purposes

- it effectively extends the entrance of the hydrogen cell beyond the manifold so that exiting particles only traverse hydrogen and thin cell walls,
- it insures that the exiting particles encounter a region that is symmetric about the beam axis, and
- it eliminates (to first order) variations in the target thickness with beam position by matching the radius of curvature of the entrance and exit windows of the hydrogen cell.

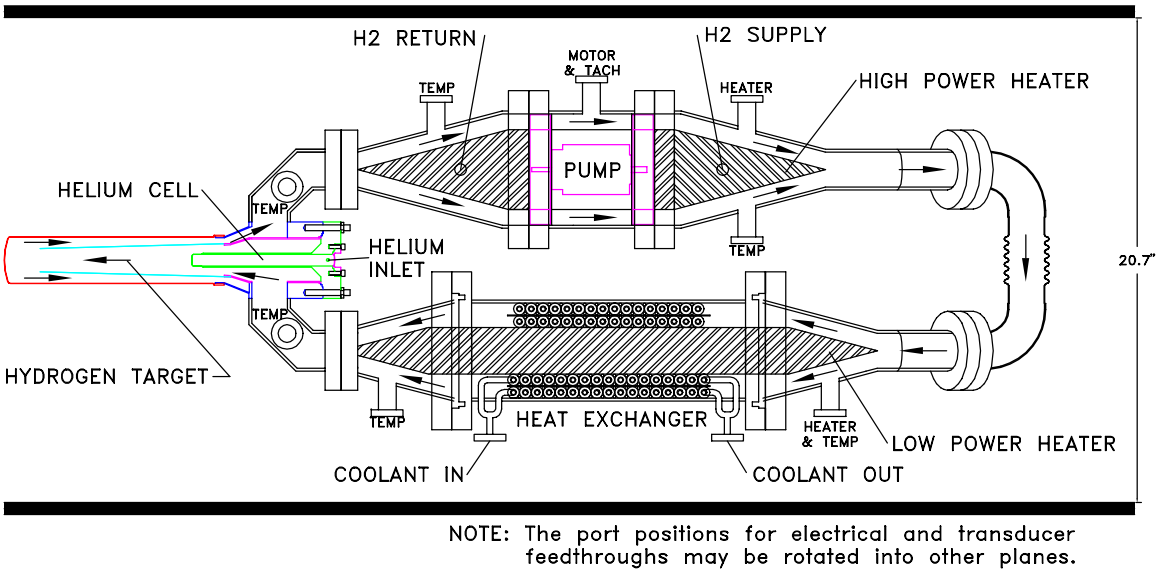

Figure 4.12: Overview of the G0 liquid hydrogen cryotarget. Beam is incident from the right in this view. Exiting scattered electrons of interest emerge at $108^\circ \pm 8^\circ$ with respect to the beam from the hydrogen liquid downstream (left in the figure) of the helium cell.

Thus the target−beam interaction region is designed to be axially symmetric and independent of beam position.

Figure 4.13 shows the details of the target cell and manifold. When the pump is running, the liquid hydrogen flows longitudinally in the same direction as the beam through the inner flow cone and returns through the annulus between the inner cone and the wall of the hydrogen cell. The distance between the exit window of the helium cell and the exit window of the hydrogen target cell is 20 cm. The holes in the inner cone are essential to prevent collapse of the cone due to Bernoulli pressure; they form an eight-fold symmetric pattern and are aligned with the G0 magnet coils so they are out of the spectrometer acceptance.

The hydrogen target cell consists of a 5 cm diameter tube with a rounded endcap, machined from a solid cylinder of 7075 aluminum. We fabricate the cell by machining the end of the cylinder flat, then pressing it in a form to make the rounded endcap. The radius of curvature of the center of the endcap is 7.6 cm. The outer side wall and endcap are 7.0 ± 0.5 mils thick. To verify that the target cell can withstand the pressure that builds up during target boiloff, each cell is hydrostatically tested to 100 psid before being soldered to the manifold. This is a factor of 2.4 safety margin over the pressure that we calculate the cell would be subjected to in a catastrophic vacuum failure.

The cryogenic loop contains two heaters, one low power and one high power, to regulate the temperature of the liquid hydrogen. These heaters are identical in function to those used in the Hall C liquid hydrogen target. The high power heater will operate at up to 1000 W maximum power with its main function being to compensate for significant

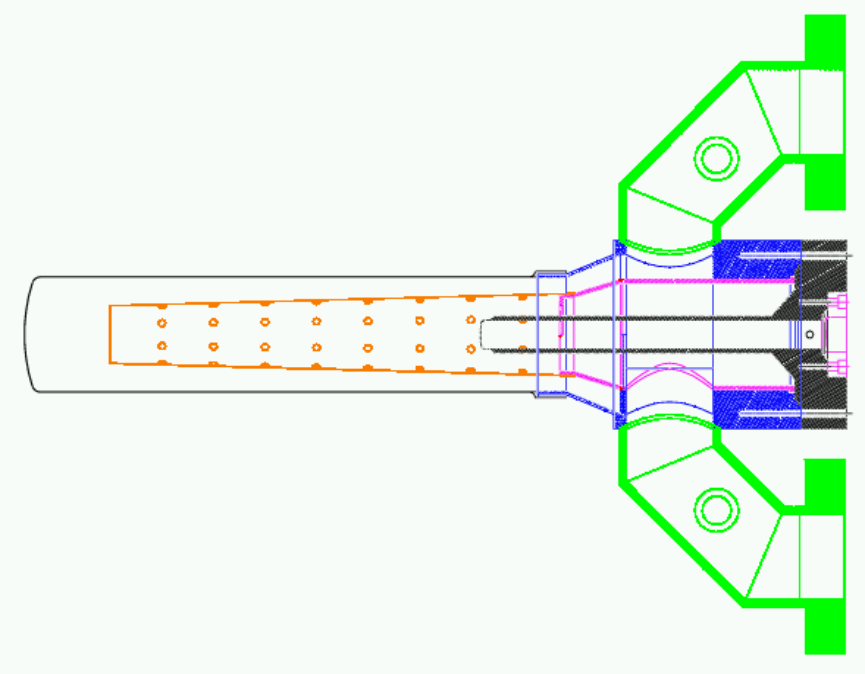

Figure 4.13: Detailed view of the G0 hydrogen target cell, helium cell and manifold. The effective hydrogen target length is 20 cm and the diameter of the outer shell of the target cell is 5 cm. In this view, hydrogen liquid enters in the lower manifold pipe and exits in the upper manifold pipe.

reductions in the beam current. The low power internal heater will be used to make relatively small adjustments to the fluid temperature and will be controlled automatically with a commercial temperature controller in a feedback loop with the temperature sensor on the upstream side of the target cell.

The loop contains a vaneaxial pump capable of displacing 4.8 l/s of liquid hydrogen. This corresponds to a mass flow rate of 333 g/s and gives a velocity in the target region of ~ 7 m/s. The pump motor is inside the cryoloop, similar to the design used in the Hall C cryotargets.

It is important to minimize density fluctuations because they introduce statistical fluctuations into the asymmetry that mask the parity violating asymmetry, requiring a longer running time to achieve the same experimental precision. To reduce resistance and maximize the circulating flow rate in the cryogenic loop we have incorporated flow diverter cones at transitions between elements of different diameters.

We expect to be able to run the backward angle measurement at 80 μA, in part because we will be using the standard 499 MHz pulse structure and in part because of the better-than-expected target performance during the forward angle run. This will help us to reduce the overall uncertainties in extracting the form factors whose uncertainties were dominated by the backward angle statistical precision. We have determined from the forward measurement that the total power handling capability will be more than sufficient for this purpose.

In addition, we estimate that the contribution of target density fluctuations to the detector asymmetry widths due to the increased power density will be less than 500 ppm even for an 80 μA beam current, as compared with the minimum statistical width of about 5000 ppm. On the other hand, we may have to shorten the target cell somewhat for the highest energy run to optimize the uncertainty – a trade-off between inelastic electron contamination and overall counting rate.

4.5 Infrastructure

Since the back-angle configuration has been planned for since the beginning of the G^0 project, many of the infrastructure and installation aspects have already been thought out or implemented. The main change is that the SMS must be moved downstream of the ferris wheel, and the SMS/ferris wheel structure must be rotated 180°. SMS rails to accommodate this configuration change have already been installed in the hall. The ferris wheel platform has been built to accommodate a corresponding (smaller) downstream shift in the ferris wheel location. We expect these rotations will be made during the August-September 2004 period.

At the time of the configuration change, the lead/polyboron beamline shielding cylinder will be removed from the ferris wheel. It is not needed in the back-angle experiment. Lead shielding will also be removed from the SMS downstream head. The ferris wheel will be rotated and the CED/Cherenkov assemblies will be added. The target service module will mate with the upstream flange of the ferris wheel, moving the target center about 3 m downstream relative to the forward-angle configuration. The SMS will be around using the same company and equipment used for the move of the SMS from Illinois to JLab. A small amount of bracing will be used to stabilize the cold mass inside the cryostat and the magnet will be slowly rotated and moved downstream to its new location.

New beamline spool pieces will be required. The downstream beam dump shielding will have to be relocated closer to the dump tunnel entrance. Techniques for placing shielding blocks in this location, outside the nominal crane radius, have already been developed and are in use.

The Møller polarimeter will need to be changed to accommodate the lower energies used in this experiment. A similar change was made successfully in the spring 2001 G_E^n experiment to accommodate Møller measurements at 0.884 GeV by moving the Møller Q1 about 6" upstream. Møller operation at 0.424 GeV will require a further upstream move; optics calculations for this configuration have been completed.

We do not expect significant changes in cyrogenic services or cabling. The cabling will probably be re-routed overhead to accomodate a somewhat longer distance to the magnet and detectors. The cryogenic services for the target will have to be supported in a somewhat different way because they are now some distance from the magnet to which they used to be affixed, but no significant problems are foreseen.

5 Organization and Schedule

As indicated above, most of the new construction for the backward angle measurements, including the CEDs, Cherenkov detectors, CED/FPD coincidence electronics, target modifications has been completed and assembly and testing is beginning. Plans for turning the experiment "around" are in place. These activities are being funded within the envelope of the original G0 project, with important additional support for the Cherenkov construction from the French (CNRS) and Canadian (NSERC) funding agencies.

We expect to complete the basic turnaround tasks at the end of this summer. It is possible that we may also install some of the new detector components at the same time. In any case we expect assembly and testing of the new components to be completely finished in time to begin re-installation of the experiment in summer 2005 for a fall 2005 run.

Our hope for completing the backward angle running is to run one Q^2 point in fall 2005 with the other two Q^2 points to be run in successive years, i.e. fall 2006 and fall 2007. We are exploring with the laboratory the possibility of combining the three runs into two longer runs (pending approval of the other Q^2 points) to save one set of installation and removal downtimes.

6 Expected Results and Beam Time Request

6.1 Expected Results

This section presents the expected results from the complete program of proposed G0 running - forward and backward hydrogen measurements and backward deuterium measurements. We have not yet decided which measurement to make with the first set of approved beam time (for which we are asking re-confirmation in this jeopardy proposal); the plan for deciding, however, is rather simple. We will make the decision based on the most interesting physics results from the forward angle measurement; the default will be to run hydrogen and deuterium targets at the highest Q^2 for practical reasons of relative ease of accelerator operation and maximum overlap with the JLab experimental program.

For the backward measurements, we have investigated in general the optimum split of time between hydrogen and deuterium running at each momentum transfer point. We show the results of this study in Figure 6.1 for the 0.3 GeV^2 point; the other momentum transfer points show a similar dependence. We conclude that an even split of running time between hydrogen and deuterium is a reasonable compromise. The even split of time for the hydrogen and deuterium running balances the uncertainties in G_E^s and G_M^s (which are minimized with about 60% of the running time on hydrogen) against those in $G_A^e(T=1)$, which are minimized at a small fraction of hydrogen running.

In our error estimates, we assume 700 hours of running time for each of the backward measurements (three on hydrogen and three on deuterium) with a 80 μA beam and 75% polarization. The assumptions we make about the uncertainties in the form factors and other quantities that go into the asymmetry calculation are summarized in Table 6.1. The expected errors on the separated form factors are summarized in Table 6.2. Figure 6.2 shows the overall uncertainties in G_E^s and G_M^s relative to the overall proton form factors G_E^p and G_M^p, and Figure 6.3 shows these uncertainties relative to two representative theoretical calculations. Figure 6.4 (also included as Figure 2.3) shows the uncertainties expected in $G_A^e(T=1)$ relative to the calculation of Zhu, *et al.* [41] where we show a comparison with the standard dipole form for G_A as measured in neutrino scattering. The contribution of the various uncertainties to the total is shown in Tables 6.3-6.5 and Figures 6.5-6.7.

6.2 Beam Time Request

At this time, we request that the PAC re-allocate the 60 days previously allocated E01-116. We also respectfully ask the PAC to reconsider the 10 days of commissioning time originally requested to establish the running conditions for the new configuration (including calibrations, background rates, etc. especially for the new CED and Cherenkov detectors) This run will require an average beam current of nominally 80 μA with the regular 499 MHz beam structure at one of the beam energies listed in Table 3.1.

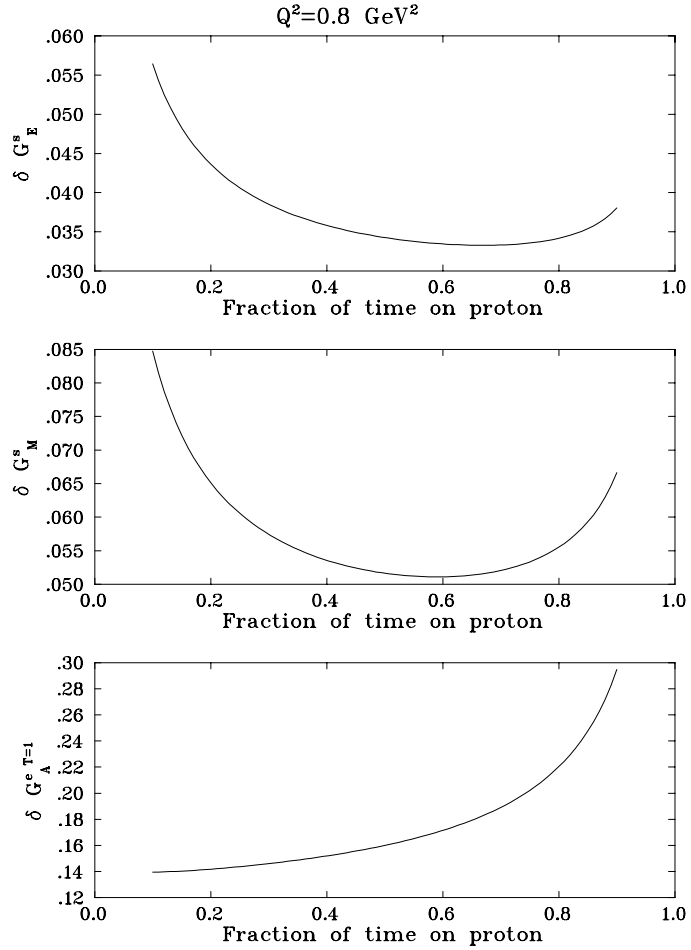

Figure 6.1: Total errors on the separated form factors at $Q^2 = 0.8$ GeV^2 as a function of the fraction of the backward angle running time on hydrogen.

Quantity	Uncertainty
$\Delta G_E^p / G_E^p$	2%
$\Delta G_M^p / G_M^p$	2%
$\Delta G_E^n / G_E^n$	20%
$\Delta G_M^n / G_M^n$	3%
$\Delta P_b / P_b$	2%
$\Delta Q^2 / Q^2$	1%
$\Delta G_A^e(T=0)$	.11
ΔR_V^p	.033
ΔR_V^n	.0004

Table 6.1: Uncertainties assumed for the quantities in the asymmetry expression. We note that present JLab experiments 93-026 and 93-038 will improve the precision of G_E^n beyond what is listed here by of order a factor of two.

Q^2 (GeV^2)	ΔG_E^s	ΔG_M^s	$\Delta G_A^e(T=1)$
0.3	0.032	0.090	0.188
0.5	0.037	0.059	0.159
0.8	0.053	0.041	0.137

Table 6.2: Expected errors on the separated form factors. These include all statistical and systematic errors.

Quantity	0.3 GeV^2	0.5 GeV^2	0.8 GeV^2
A_f	.020	.027	.046
A_b	.013	.014	.017
A_d	.008	.008	.008
G_E^p	.005	.005	.004
G_M^p	.005	.005	.004
G_E^n	.012	.012	.009
G_M^n	.003	.003	.002
Q^2	.007	.008	.008
P_e	.012	.013	.013
$others$	.004	.004	.003
total	.032	.037	.053

Table 6.3: Contributions to the error on G_E^s. The entries for Q^2 and P_e include the errors for all three measurements(f, b, d) added in quadrature. The "others" entry includes $G_A^e(T=0), R_V^p, R_V^n$.

Quantity	0.3 GeV^2	0.5 GeV^2	0.8 GeV^2
A_f	.007	.005	.004
A_b	.055	.035	.025
A_d	.038	.024	.018
G_E^p	.000	.000	.000
G_M^p	.011	.008	.006
G_E^n	.007	.004	.002
G_M^n	.014	.011	.008
Q^2	.028	.019	.012
P_e	.047	.032	.020
$others$	.019	.011	.007
total	.090	.059	.041

Table 6.4: Contributions to the error on G_M^s. The entries for Q^2 and P_e include the errors for all three measurements(f, b, d) added in quadrature. The "others" entry includes $G_A^e(T=0), R_V^p, R_V^n$.

Quantity	0.3 GeV^2	0.5 GeV^2	0.8 GeV^2
A_f	.034	.034	.045
A_b	.014	.010	.010
A_d	.120	.098	.090
G_E^p	.023	.011	.005
G_M^p	.015	.018	.016
G_E^n	.022	.016	.010
G_M^n	.043	.033	.023
Q^2	.066	.056	.043
P_e	.111	.096	.076
others	.012	.010	.007
total	.188	.159	.137

Table 6.5: Contributions to the error on $G_A^e(T=1)$. The entries for Q^2 and P_e include the errors for all three measurements(f, b, d) added in quadrature. The "others" entry includes $G_A^e(T=0), R_V^p, R_V^n$.

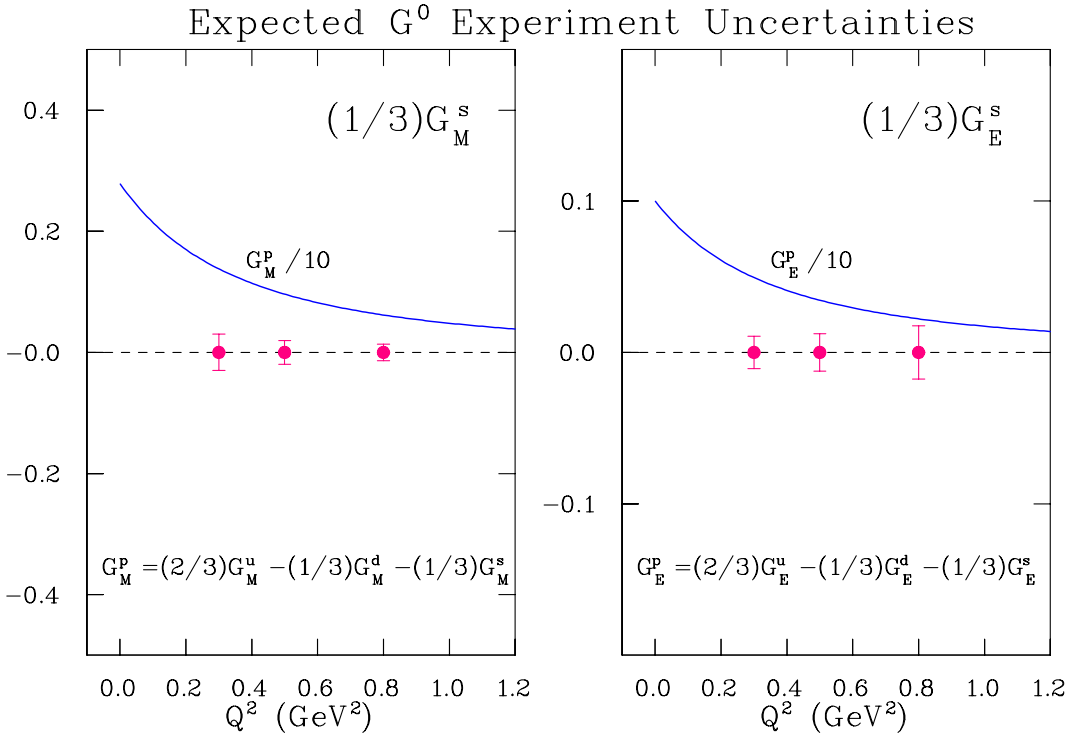

Figure 6.2: Expected errors on the contribution of the strange form factors to the electric and magnetic proton form factors.

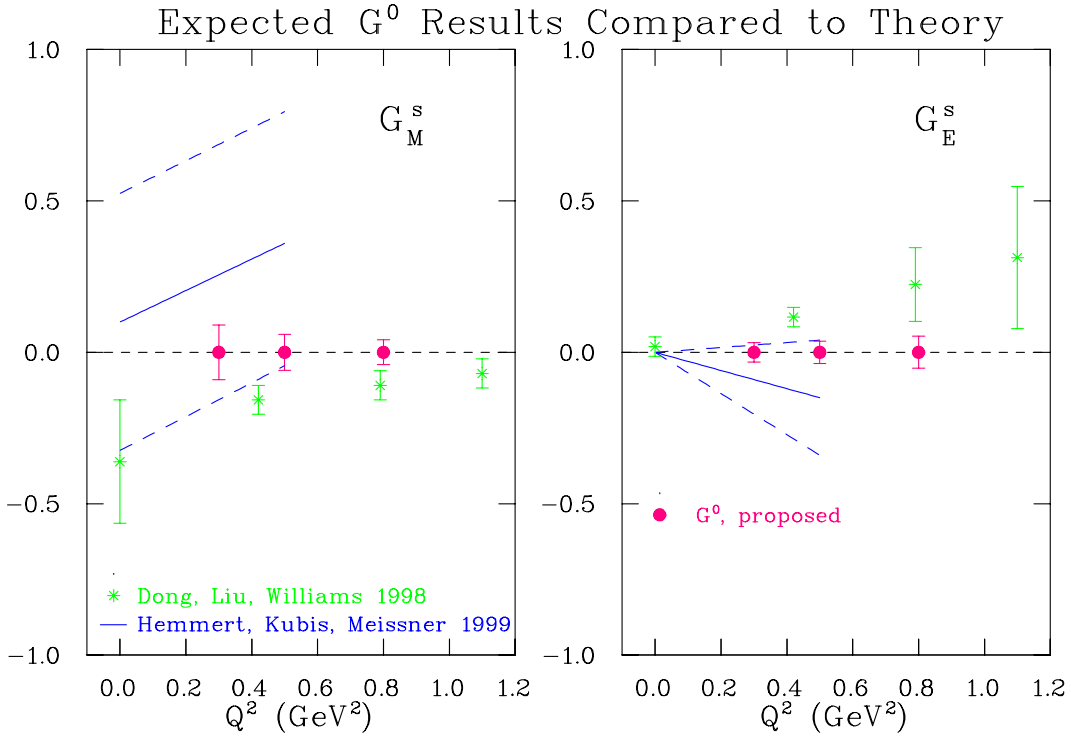

Figure 6.3: Expected G^0 errors compared to a lattice gauge theory prediction (Dong, *et al.*) and a chiral perturbation theory prediction (Hemmert, *et al.*).

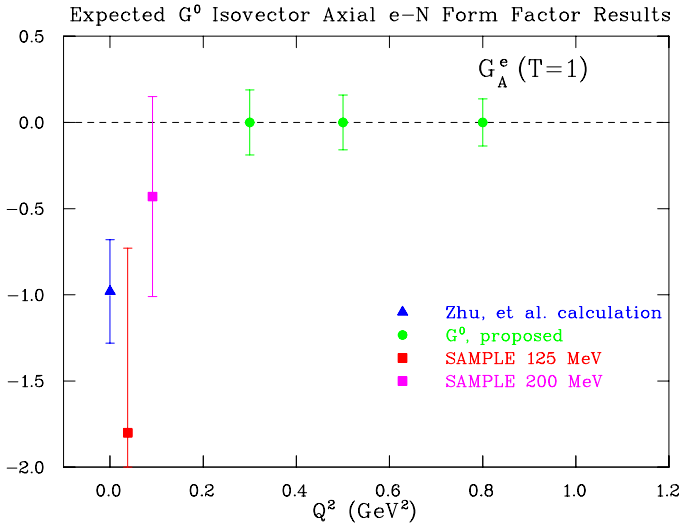

Figure 6.4: Expected errors on the isovector axial e-N form factor.

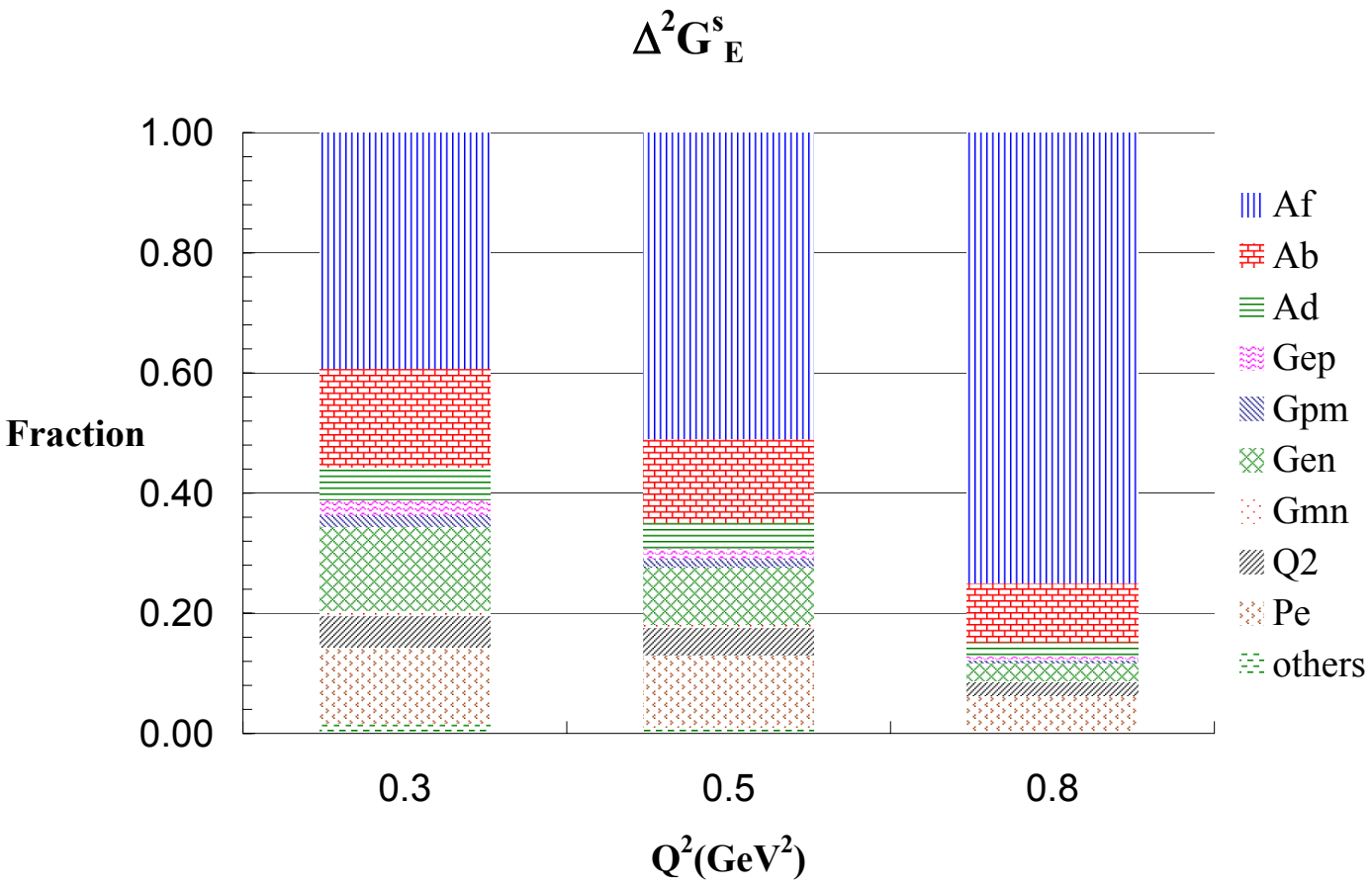

Figure 6.5: Fractional contributions to the error on $\Delta^2 G_E^s$. The entries for Q^2 and P_e include the errors for all three measurements(f, b, d) added in quadrature. The "others" entry includes $G_A^e(T=0), R_V^p, R_V^n$.

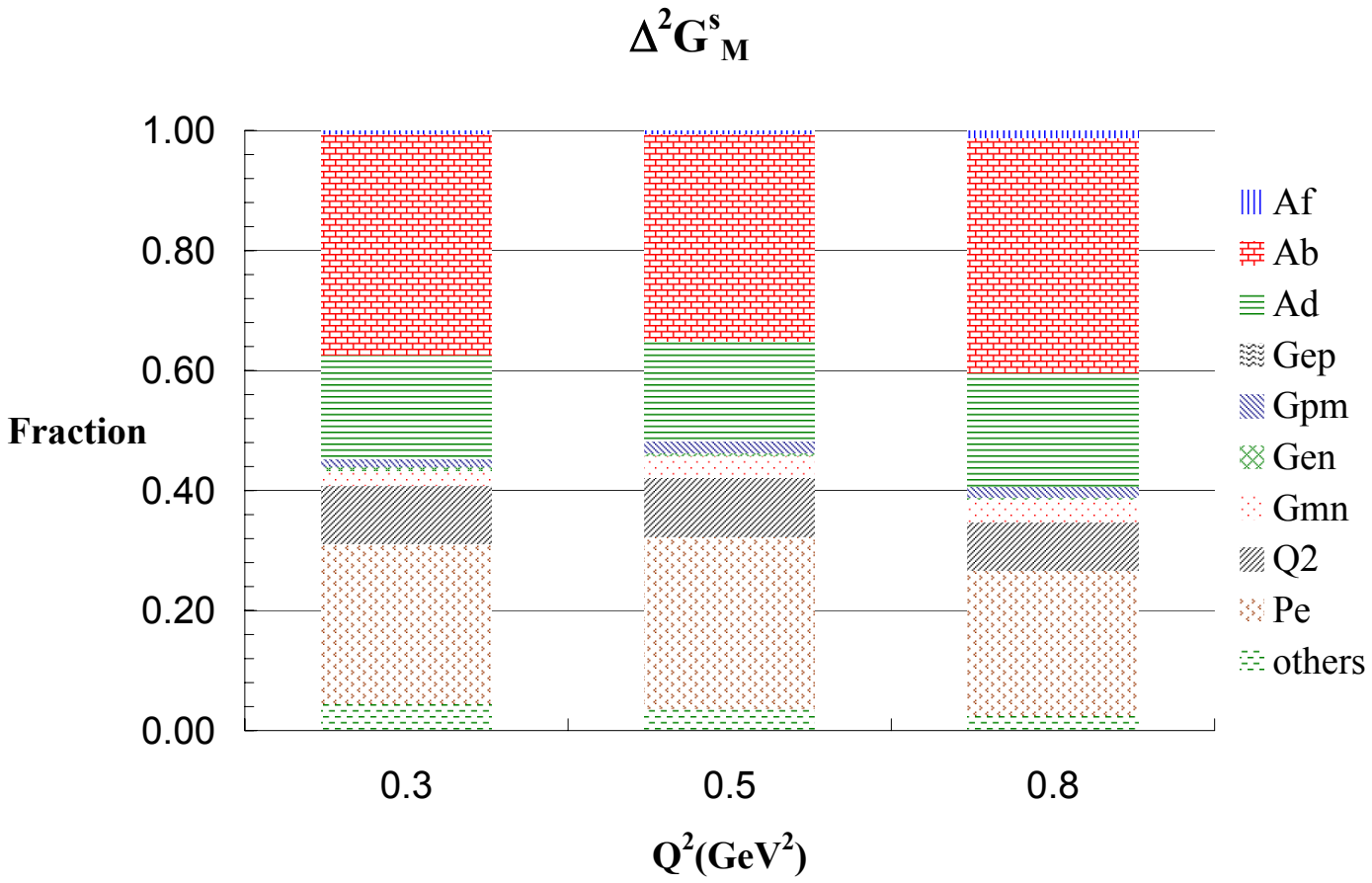

Figure 6.6: Fractional contributions to the error on $\Delta^2 G^s_M$. The entries for Q^2 and P_e include the errors for all three measurements(f, b, d) added in quadrature. The "others" entry includes $G^e_A(T=0), R^p_V, R^n_V$.

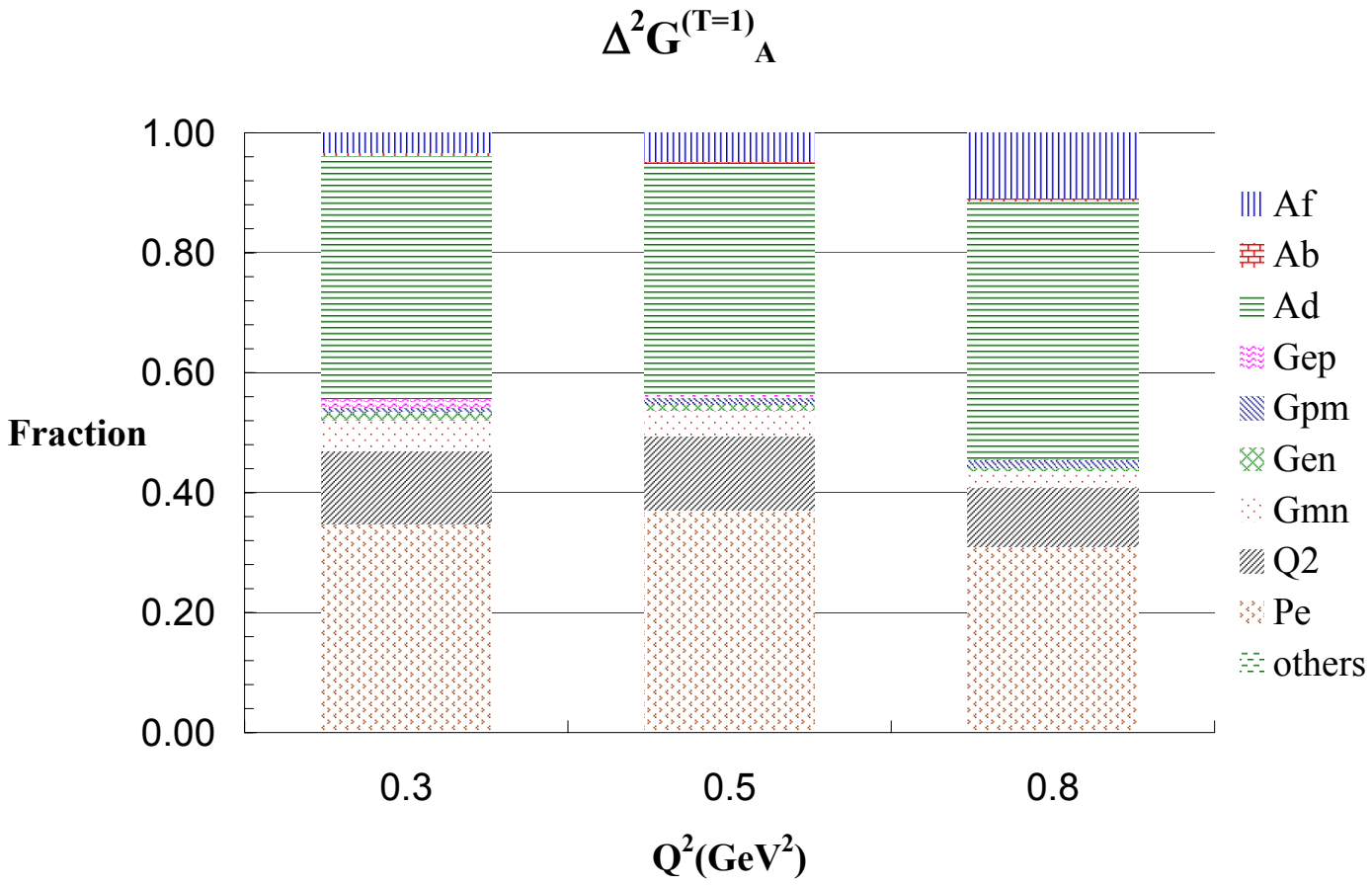

Figure 6.7: Fractional contributions to the error on $\Delta^2 G_A^e(T=1)$. The entries for Q^2 and P_e include the errors for all three measurements(f, b, d) added in quadrature. The "others" entry includes $G_A^e(T=0), R_V^p, R_V^n$.

References

[1] D. H Beck and R. D. McKeown, Ann. Rev. Nucl. Part. Sci. **51** 189 (2001).
[2] D. Kaplan and A. Manohar, *Nucl. Phys. B* 310, 527 (1988).
[3] R. D. McKeown, *Phys. Lett.* B219, 140 (1989).
[4] D. H Beck, *Phys. Rev.* D39, 3248 (1989).
[5] M. J. Musolf, *et al.,*, *Phys. Rep.* 239 1 (1994).
[6] M. J. Musolf and B. R. Holstein, *Phys. Lett.* B242, 461 (1990).
[7] E. Hadjimichael, G. I. Poulis, and T. W. Donnelly, Phys. Rev. **C45**, 2666 (1992).
[8] L. Diaconescu, R. Schiavilla, and U. van Kolck, Phys. Rev. **C6304**, 4007 (2001).
[9] C. Liu, G. Prezeau and M. Ramsey-Musolf, Phys. Rev. **C67** 035501 (2003).
[10] T. Ito, *et al.*, Phys. Rev. Lett. **92** 102003 (2004).
[11] Particle Data Group, *Euro. Phys. J.* **C54**, 1 (2000).
[12] H. Gao, Int. J. Mod. Phys. E **12**, 1 (2003).
[13] G. A. Miller, Phys. Rev. **C57**, 1492 (1998).
[14] W. J. Marciano and A. Sirlin, Phys. Rev. **D27**, 552 (1983); W. J. Marciano and A. Sirlin, Phys. Rev. **D29**, 75 (1984).
[15] M. J. Musolf and M. Burkardt, *Z. Phys.* C61, 433 (1994).
[16] W. Koepf, E. M. Henley, and S. J. Pollock, *Phys. Lett.* B288 11 (1992).
[17] B. R. Holstein in *Proceedings of the Caltech Workshop on Parity Violation in Electron Scattering*, E. J. Beise and R. D. McKeown, Eds., World Scientific, 27 (1990).
[18] H. Ito, *Phys. Rev.* C52, R1750 (1995).
[19] P. Geiger and N. Isgur, Phys. Rev. **D55**, 299 (1997).
[20] L. Hannelius and D.-O. Riska, Phys. Rev. **C62**, 045204 (2000); L. Hannelius, D.-O. Riska, and L.-Y. Glozman, Nucl. Phys. **A665**, 353 (2000).
[21] R. L. Jaffe, *Phys. Lett.* B229, 275 (1989).
[22] H.-W. Hammer, U.-G. Meissner, and D. Drechsel, *Phys. Lett.* B367, 323 (1996).
[23] U.-G. Meissner *et al.*, preprint hep-ph/9701296.
[24] M. J. Musolf, H.-W. Hammer, and D. Drechsel, *Phys. Rev.*. **D55** 2741 (1997).
[25] N. W. Park, J. Schechter, and H. Weigel, *Phys. Rev.* D43, 869 (1991).
[26] S. Hong and B. Park, *Nucl. Phys.* A561, 525 (1993).
[27] C. V. Christov, *et al., Prog. Part. Nucl. Phys.* 37, 1 (1996).
[28] S-T. Hong, B-Y. Park, and D-P. Min, preprint nucl-th/9706008.
[29] S. J. Dong, K. F. Liu, and A. G. Williams, Phys. Rev. D **58**, 074504 (1998).
[30] D. B. Leinweber and A. W. Thomas, Phys. Rev. D **62**, 074505 (2000).
[31] D. B. Leinweber, *et al.*, JLAB-THY-04-8.
[32] H. Weigel, *et al.*, *Phys. Lett.* B353, 20 (1995).

[33] D. H. Beck and B. R. Holstein, Int. J. Mod. Phys. **E10** 1 (2001).
[34] S. C. Phatak and Sarira Sahu, *Phys. Lett.* **B321** 11 (1994).
[35] D. Leinweber, *Phys. Rev.* D53, 5115 (1996).
[36] M. J. Ramsey-Musolf and H. Ito, *Phys. Rev.* **C55**, 3066 (1997).
[37] M. J. Musolf, Ph.D. thesis, Princeton University, unpublished.
[38] I. Zel'dovich, JETP Lett. **33**, 1531 (1957).
[39] W. C. Haxton, E. M. Henley, and M. J. Musolf, Phys. Rev. Lett. **63**, 949 (1989); W. Haxton, Science **275**, 1753 (1997).
[40] C. S. Wood *et al.*, Science **275**, 1759 (1997).
[41] S.-L. Zhu, *et al.*, Phys. Rev. **D62**, 033008 (2000).
[42] D.-O. Riska, Nucl. Phys. **A678**, 79 (2000).
[43] C. M. Maekawa and U. van Kolck, Phys. Lett. **B478**, 73 (2000).
[44] C. M. Maekawa, J. S. Viega, and U. van Kolck, Phys. Lett. **B488**, 167 (2000).
[45] B. A. Mueller *et al.*, *Phys. Rev. Lett.* 78, 3824 (1997).
[46] B. A. Mueller, Ph.D. thesis, California Institute of Technology, unpublished.
[47] T. A. Forest, Ph.D. thesis, University of Illinois at Urbana-Champaign, unpublished.
[48] D. P. Spayde, Ph. D. thesis, University of Maryland, unpublished.
[49] D. T. Spayde *et al.*, Phys. Rev. Lett. **84**, 1106 (2000).
[50] D. Spayde, *et al.*, Phys. Lett. **B58** 79 (2004).
[51] T. R. Hemmert, U.-G. Meissner, and S. Steininger, Phys. Lett. **B437** 184 (1998).
[52] MIT-Bates Lab experiment 00-04, T. Ito, spokesperson.
[53] K.A. Aniol et al. (HAPPEX Collaboration), Phys. Rev. Lett. **82**, 1096 (1999).
[54] K. A. Aniol, et al. (HAPPEX Collaboration), nucl-ex/00060002.
[55] F. Maas, *et al.*, submitted to Phys. Rev. Lett. arXiV nucl-ex/0401019.
[56] Jefferson Lab experiment 99-115, K. Kumar and D. Lhuillier, spokespersons.
[57] Jefferson Lab experiment 00-003, R. Michaels, P. Souder and R. Urciuoli, spokespersons.
[58] Jefferson Lab experiment 00-114, D. Armstrong, spokesperson.
[59] Jefferson Lab experiment 91-004, E. Beise, spokesperson
[60] Mainz experiment PVA4, D. von Harrach, spokesperson; F. Maas, contact person.
[61] S. Schramm and C. Horowitz, Phys. Rev. **C49**, 2777 (1994).
[62] Kuster and Arenhövel, Nucl Phys. **A626**, 911 (1997).
[63] W.Y.P. Hwang, E.M. Henley, and G.A. Miller, Ann. Phys. **137**, 378 (1981).
[64] B. Desplanque, J.F. Donoghue, and B.R. Holstein, Ann. Phys. **124**, 449 (1980).
[65] S. Pollock, Phys. Rev. **D42**, 3010 (1990).
[66] S. Wells, JLab experiment E97-104.
[67] N. Mukhopadhyay, *et al.*, Nucl. Phys. **A633**, 481 (1998).
[68] P. Amore *et al.*, Los Alamos preprint nucl-ex/0007072.
[69] D. Drechsel, O. Hanstein, S.S. Kamalov and L. Tiator, Nucl. Phys. **A645** (1999) 145.
[70] L. Tiator and L. E. Wright, Nucl. Phys. **A379** (1982) 407.

[71] R. Tieulent and J-S. Réal, *Test of a Photoproduction Generator Using the SOS data of December 1999*, G^0 Technical Report G0-00-019 (July 12, 2000).
[72] J. L. Matthews and R. O. Owens, Nucl. Instrum. Meth. **111** (1973) 157.
[73] J. W. Lightbody Jr. and J. S. O'Connell, Computers in Physics. **May/June** (1988) 57.
[74] R. Tieulent, P. King, A. Lung, J. Martin, M. Pitt, J-S. Réal, J. Roche, Gr. Smith, Gw. Smith, and V. Tadevosyan, *Experimental Background Contributions to the G^0 Backward Angle Measurements*, G^0 Technical Report G0-01-012 (April 21, 2001).
[75] E. Rollinde, *G0GEANT Manual (DRAFT)*, G^0 Technical Report G0-99-035 (June, 1999).
[76] S. P. Wells, N. Simicevic, K. Johnston, and T. A. Forest, and The G^0 Collaboration, *PAC20 Proposal: Measurement of the Parity Violating Asymmetry in the N-¿DELTA Transition (Originally E97-104)*
[77] S.P. Wells, G0-99-008, LATECH-CAPS-99-03b (1999).
[78] C. Murphy, S.P. Wells, and N. Simicevic, G0-99-051, LATECH-CAPS-99-11a (1999).
[79] G. Quéméner and S. Kox, *Aerogel Cherenkov Counter Design for the G0 Spectrometer*, G^0 Technical Report G0-00-052 (December 13, 2000).
[80] J. W. Martin, *Aerogel Cherenkov Counter Design*, G^0 Technical Report G0-00-054 (June 12, 2000).
[81] D. Higinbotham, Nucl. Instrum. and Meth. **A414** (1998) 332.

7 Appendix A: G0 Commissioning Certification Report, March 2004

8 Appendix B: Summary of Leakage Beam Asymmetry Effect in Forward Angle Measurement

In running with reduced Hall C beam current (associated with deadtime studies) at the time when Hall A was coming back on after magnet repairs in April 2004, we discovered a false asymmetry coming from "leakage" beam current. In this Appendix we present our preliminary conclusions about the sources and solutions for the leakage asymmetry problem. The source of the leakage current is the d.c. level of light from all three lasers used to generate the Halls A, B and C beams in the polarized source. Because all three lasers utilize a laser amplifier, there is essentially d.c. "Amplified Spontaneous Emission" (ASE) light generated even when the seed laser beam is not present. This light produces in Hall C a low current 499 MHz "leakage" beam in addition to the 31 MHz primary beam desired for the experiment. It turns out that the charge asymmetry of the leakage beam can be large on our scale ($\sim 100 - 1000$ ppm) and even though its current is ~ 40 nA, the combined effect is significant. We present here a preliminary analysis of this effect. *It is important to note that this effect will not affect the backward angle measurement as it results from the different time structure of the Hall C beam relative to Halls A and B – we will run the backward angle experiment with the same time structure.*

The easiest way to understand how the leakage beam affects our data is to consider the feedback on the beam current asymmetry. Our beam current monitors see the whole beam (499 MHz leakage and 31 MHz primary) and we feed back to the polarized source to force the helicity-correlated current asymmetry to zero. However, because the leakage beam is included in the measurement, the current asymmetry of our 31 MHz beam is forced to a non-zero value in order to cancel the current asymmetry of the leakage beam. The resulting current asymmetry of the 31 MHz beam generates a false asymmetry in the detector signal for the elastic protons.

We performed a number of tests at the conclusion of the forward angle run to quantify the contributions and to develop a strategy for correcting their effects. It is important to first understand the magnitude of these effects. When running with just Hall B (the majority of the forward angle data), the leakage asymmetries were of order 500 ppm or less and the leakage currents of 20 - 40 nA. The false asymmetry for the elastic protons is, to a very good approximation, just the asymmetry of the main beam given by

$$A_f = \frac{I_{leak}}{I_C} A_{leak} = \frac{40\text{nA}}{40\mu\text{A}} 500\text{ppm} = 0.5\text{ppm} \tag{8.1}$$

For the Hall A running the leakage asymmetries were as much as $\sim 10\times$ larger although the Hall A leakage current is typically a factor of 2-4 smaller in our measurements (lower level of ASE as expected). For the moment we are concentrating on correcting the data taken

with just Hall B running. We believe we can make a correction for this false asymmetry with ~ 0.1 ppm or 10-20% precision.

Our measurements show that the leakage currents and asymmetries are not stable, changing on time scales of hours. Therefore our strategy is to use data taken concurrently with our elastic proton asymmetry data to determine the rate and asymmetry of the leakage current. Tests performed at the end of the forward angle run were used to verify that this approach gives the correct results at the 10-20 % level. In these tests, the luminosity monitors allowed us to make very accurate, direct measurements of the leakage current asymmetry (the standard current monitors do not have enough sensitivity) which could be compared with the detector measurements to be used to correct the elastic asymmetries. We therefore measured the leakage currents of the Halls A, B and C beams independently* and in various combinations as part of this verification.

The detector data include a region in our t.o.f. spectrum ("cut 0") where we are sensitive to the yield and asymmetry of the leakage beam. After the slowest protons have reached the focal surface and before the $\beta = 1$ particles from the next beam pulse can reach the detectors, there is a period of a few ns in which we see the leakage beam. There is also a background component in this region, due to the main Hall C beam which we interpret to be due to the "gas" of neutrons and possibly gammas that builds up in the Hall. This component is measured to have a relatively small asymmetry, and the rate is proportional to the primary beam current. Table 8.1 summarizes representative contributions to the leakage currents and asymmetries.

Component	Current (nA)	Asymmetry (ppm)
Hall A	10	1000-5000
Hall B	35	500
Hall C	10	200
Hall C (bkgd)	110	< 100

Table 8.1: Typical beam currents and asymmetries for contributions to cut 0. The Hall C background "beam current" is an equivalent current based on the rates measured in cut 0: about 2/3 of the cut 0 rate is due to this background, 1/3 is due to leakage current.

An example of our test technique is shown in Figure 8.1. As part of our testing, we made standard one hour asymmetry measurements, interleaved with leakage measurements using the luminosity monitors. From the direct leakage measurements we can calculate the expected cut 0 asymmetry and compare with what is measured (in the analysis of the actual data, the procedure is reversed). In Fig. 8.1, we have considered the more difficult situation case with both Halls A and B on, and two measurement periods separated by about 1 day. With the A+B leakage asymmetry measured by the luminosity monitors of $+1037 \pm 19$ ppm (shown) and the measured Hall C leakage asymmetry of about -100 ppm,

*Leakage from Halls A and B is measured in a straightforward way by measuring with just one of the other Halls on and with the Hall C laser off. The Hall C leakage beam is measured separately by directing the Hall C beam to the Hall A or B chopper slit.

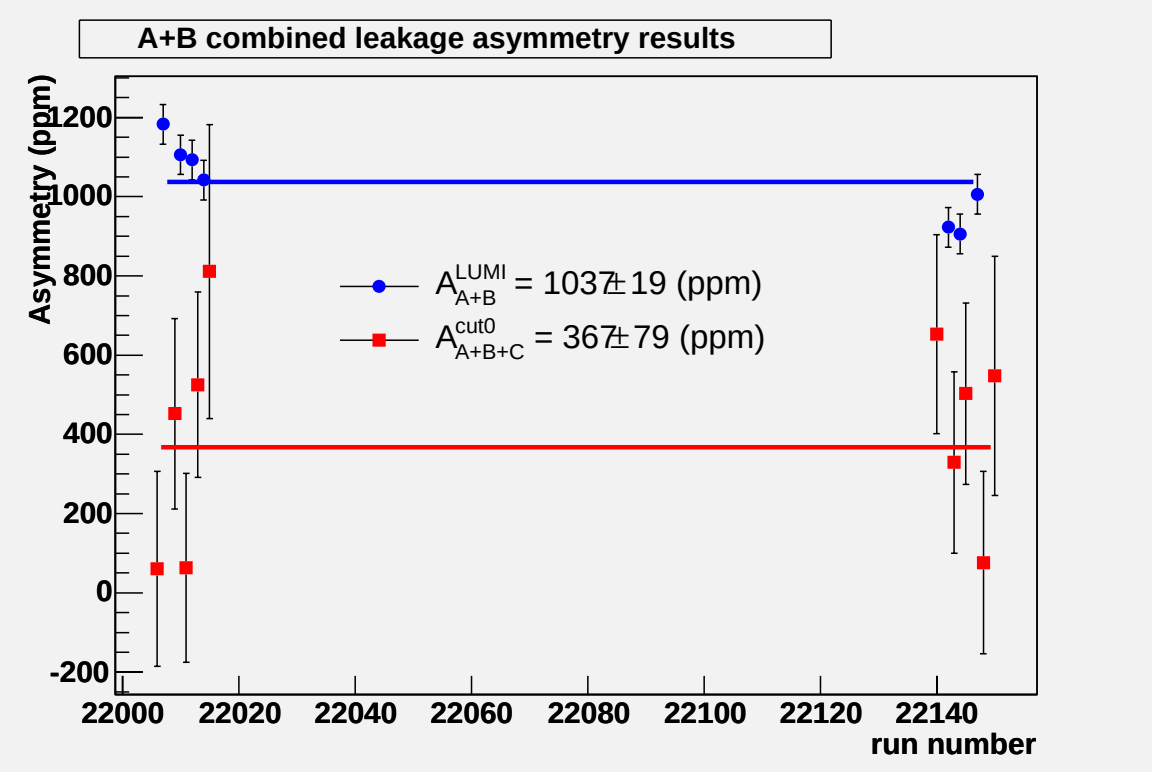

Figure 8.1: Direct measurement of the leakage beam asymmetry and corresponding asymmetries in the cut 0 region of the t.o.f. spectrum as discussed in the text.

we can calculate the asymmetry expected in cut 0 of about 340 ppm in agreement with the cut 0 measurement at the 20% level. We believe that a combination of the measurements made during this period will allow us to verify the technique at the desired 10% or 0.1 ppm level (the statistical precision of the cut 0 asymmetries in the example given are limited – we recorded significantly more data which have not yet been analyzed). Further, based on this set of standard measurements, and in the context of the overall experiment, the statistical precision in the cut 0 region is sufficient to make determinations of the average false asymmetry due to leakage at the 0.1 ppm level for every $\sim$ 40 hours of data.